# Chapter 7
# Shock Wave Interaction with Gaseous Interface


## 7.1 Introduction

Shock wave interaction with a gaseous interface is one of basic topics of the shock wave research (Abd-el-Fattah et al. 1978). Figure 7.1 shows a triangular shaped container accommodating a foreign gas interface. The foreign gas was tightly sealed in the container with a 30 μm thick Mylar membrane. The container was installed in the 60 mm × 150 mm conventional shock tube. A foreign gas was circulated through a supply system shown in Fig. 7.1 at the pressure slightly higher than the test pressure and circulated continuously for several minutes. Eventually the value of the foreign gas pressure was adjusted with the test gas pressure. Hence the level of impurity of the foreign gas was minimized by elongating the circulation period of time. The averaged level of the impurity was less than a few %.

The effect of the Mylar membrane on shock wave reflection is shown in Fig. 7.2. The shock wave propagates over a 45° air/air interface for Ms = 1.20. The IS passed through the interface without causing any disturbances. But the Mylar membrane was bent toward inward but the reflected shock wave pattern from the interface was a RR.

### *7.1.1 Air/He Interface*

The reflection from the air/helium interface is called as the slow/fast interaction and that from the air/$CO_2$ interface is called as the fast/slow interaction. Figure 7.3 show the evolution of shock wave reflection from the air/helium interface for Ms = 1.20. The slow/fast interaction is analogous to the shock wave in air reflected from the water wedge.

Waves in the helium layer propagate at the sound speed in helium and hence are observed as the faint change of contrast. The speed of the shock wave propagating



K. Takayama, *Visualization of Shock Wave Phenomena*,
https://doi.org/10.1007/978-3-030-19451-2_7

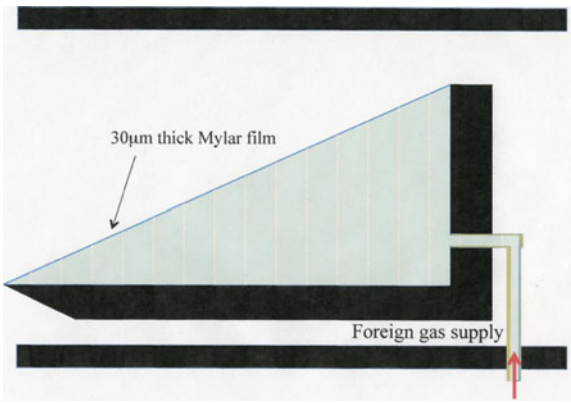


**Fig. 7.1** The test section of a foreign gas interface installed in the 60 mm × 150 mm shock tube

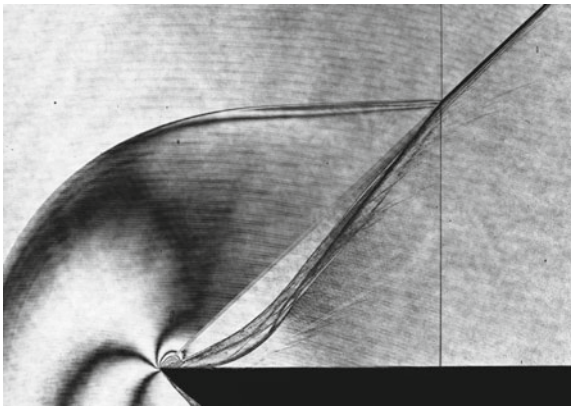

**Fig. 7.2** Shock wave propagation over air/air interface at angle of 45° #93070101 for Ms = 1.198 in atmospheric air at 297.3 K

along the interface whose inclination angle is $\theta_w$ is defined as $u_{inter} = u_s/\cos\theta_w$, where $u_s$ is the speed of the incident shock wave IS. Therefore, if the interface angle satisfies the condition of $\theta_w < \cos^{-1}(u_s/a_{helium})$, where the $a_{helium}$ is the sound speed in helium, the compression waves induced by the IS propagate in helium head the IS.

In Fig. 7.3a, if the interface was a solid wedge, the reflection pattern should be a vNMR and the resulting triple point trajectory angle should be the glancing incidence angle $\theta_{glance}$, of 25.5°. In the reflection from the present slow/fast interface, as seen in Fig. 7.3a it is larger than this value. In addition to this, the MS so far observed in Fig. 7.3a is not perpendicular to the interface but slightly tilted backward. It is clearly observed that the reflected shock wave from the interface behaved differently from that of a vNMR over solid wedges. As the disturbances propagated in helium at $a_{helium}$ faster than the movement of the foot of the IS, it lifted up the interface slightly upward resulting in oblique fringes which are terminated at the MS. The presence of leading fringes uniquely appeared over this slow/fast interface but was not observed over the water wedges. The underwater shock wave

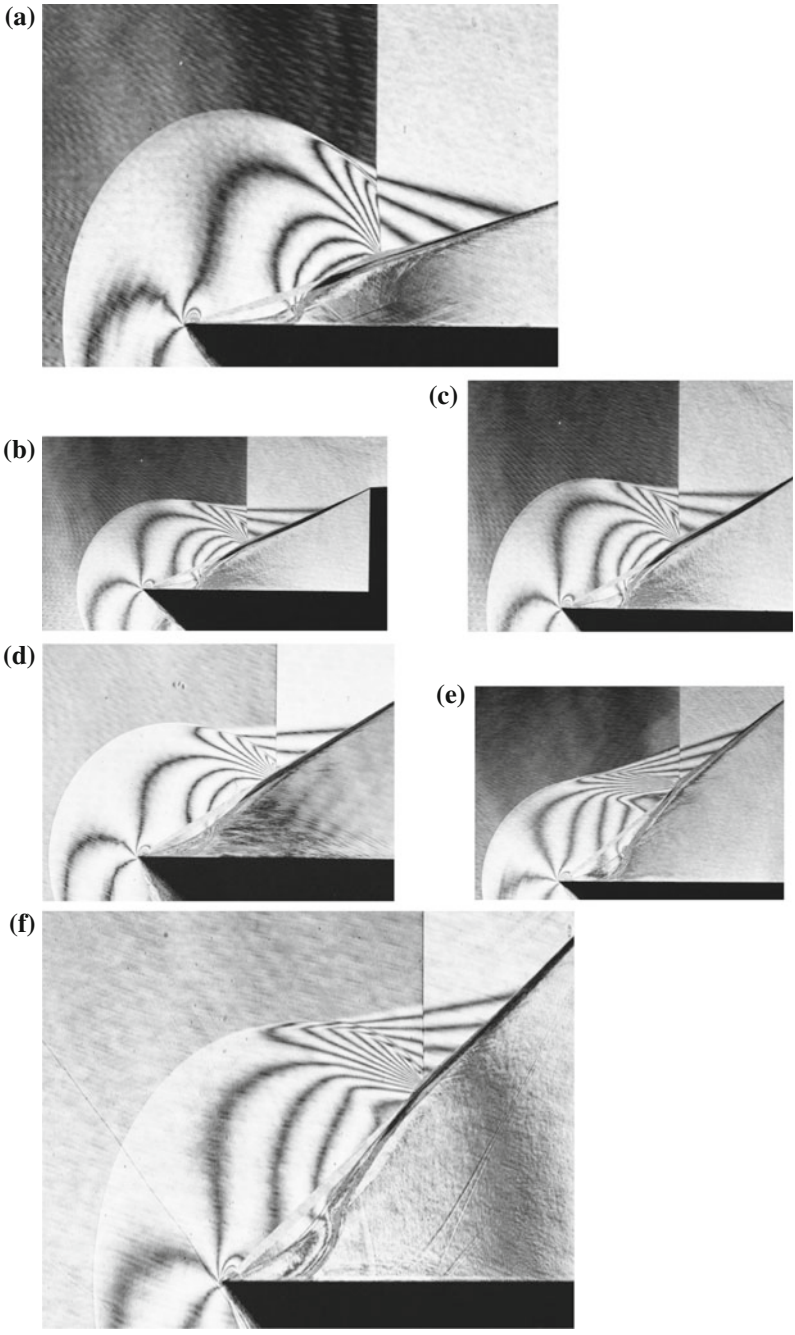


**Fig. 7.3** Shock wave interaction with air/He interface, exchange time 10 min, Ms = 1.20 in atmospheric air at 297 K: **a** #93053108, Ms = 1.199, $\theta_w = 15°$; **b** #93052807, Ms = 1.203, $\theta_w = 25°$; **c** #93052801, Ms = 1.200, $\theta_w = 30°$; **d** #93053102, Ms = 1.200, $\theta_w = 35°$; **e** #93053103, Ms = 1.203, $\theta_w = 40°$; **f** #93052603, Ms = 1.207, $\theta_w = 44.6°$

propagation over a brass wall was a shock wave interaction with the slow/first interface, the stress waves were released from the brass wall to water.

A triple point, TP, formed on the reflected shock wave seen in Fig. 7.3a does not accompany a slip line SL. This reflection pattern is similar to a vNMR. When the interface angle $\theta_w$ approached to the critical transition angle, $\theta_{crit}$, the TP approached to the interface and eventually MS terminated as seen in Fig. 7.3c, d. The precursory oblique fringes in air are observed and terminated on the reflected shock wave. When the $\theta_w \geqq \theta_{crit}$ is satisfied, the pattern of the reflected shock wave becomes a MR.

With increasing $\theta_w$, when $u_{inter}$ exceeds the $a_{helium}$, the compression waves created by the IS in helium coalesced into a weak oblique shock wave. This situation was closely related to the level of compression wave induced in the helium layer. Practically the situation was linked with the degree of deformation of the Mylar membrane. During the series of experiments conducted in May 1993 as presented in Fig. 7.3, the membrane deformed slowly in a controlled manner generating compression waves in the helium layer. Therefore, the head of the train of compression waves was not distinctly observed in Fig. 3.3. However, in the series of the experiments conducted in November 1990, the Mylar deformed and even ruptured in a uncontrolled manner. Hence the head of the train of compression waves became clearly visible in Fig. 7.4, whereas it was hardly observable in Fig. 7.3.

During the experiments of the foreign gas interface, the experiments were conducted in a facility having a circular test section connected to a horizontal cookie cutter but the test section was relatively loosely sealed with the Mylar membrane. Hence, at the impingement of the IS, the Mylar membrane deformed very largely.

Figure 7.4a shows the shock wave reflection from the air/helium interface at the interface angle of 25° for Ms = 1.40. The reflected shock wave pattern was a SMR and the TP accompanied the SL. However, the SL was not perpendicular to the interface but slightly tilted backward. When the IS impinged the interface, the resulting compression waves was running ahead of the IS. The compression waves precursory to the IS lifted the interface upward generating the precursory fringes in air.

Figure 7.4a explains the wave propagating in the helium layer. In Fig. 7.3, the membrane sustained the pressure behind the IS and deformed slightly inward. In Fig. 7.4, after the first deformation of the membrane, it deformed violently and drove an oblique shock wave. An oblique shock wave appeared from the foot of the MS to the leading edge of the interface. The oblique shock wave was reflected from the bottom wall. With increasing the $\theta_w$, the foot of the IS approaches gradually to the precursory shock wave as shown in Fig. 7.4e. In Fig. 7.4f, the foot of the IS merged with the precursory wave in helium. The $\theta_{crit}$ of the air/helium interface would depend on the helium impurity. When $\cos\theta_w = u_s/a_{helium}$ is achieved, as seen in Fig. 7.4f, the transition to a RR occurs.

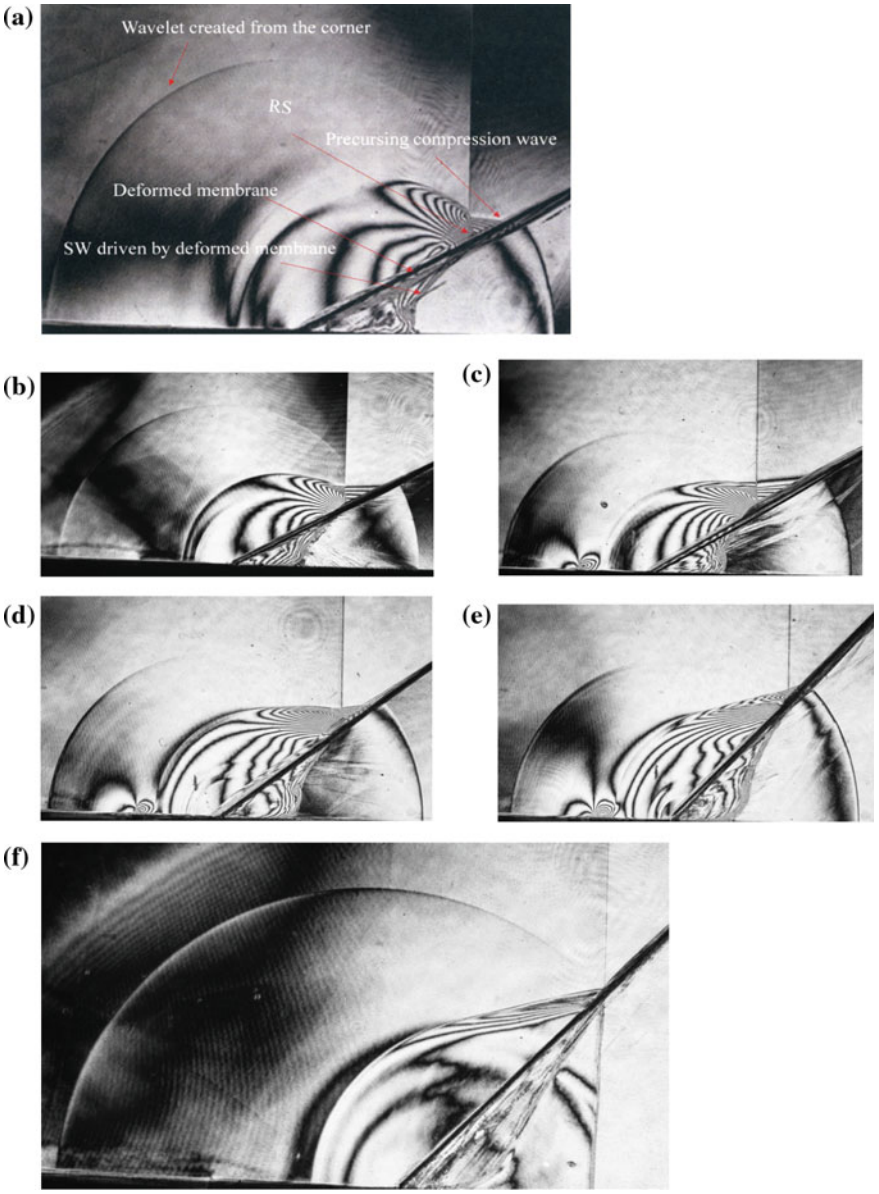


**Fig. 7.4** The interaction of shock wave with air/helium interface, 10 min duration of time for circulating helium, for Ms = 1.40 in atmospheric air at 290.9 K: **a** #90111505, Ms = 1.405, $\theta_w = 25°$; **b** #90110901, Ms = 1.418, $\theta_w = 30°$; **c** #90111402, Ms = 1.391, $\theta_w = 30°$; **d** #90110903, Ms = 1.401, $\theta_w = 37°$; **e** #90110904, Ms = 1.399, $\theta_w = 45°$; **f** #90111503, 140 us, Ms = 1.405, $\theta_w = 47°$

### 7.1.2 *Air/$CO_2$ Interface*

Figure 7.5 show the evolution of shock waves interacting with air/$CO_2$ interface. The interface angles vary from 15° to 55° for Ms = 1.20. This is a fast/slow interaction: the sound speed in $CO_2$ is 280 m/s at 293 K and that in air is 345 m/s at 290 K. The oblique shock wave is generated in the slow gas. At a shallower interface angle as seen in Fig. 7.5a, b, the TP does not accompany a SL. The reflected shock wave pattern is vNMR but the MS slightly leaned forward. However, in Fig. 7.5d at $\theta_w$ = 30°, the transition already took place and the pattern of the reflected shock wave was a RR. In Fig. 7.5e at $\theta_w$ = 35°, the pattern of the reflected shock wave was a SuRR.

An oblique shock wave was formed in $CO_2$ and reflected from the bottom wall. The reflection patterns was always a SMR as shown in Fig. 7.5a–d. However, with increasing $\theta_w$, its triple point gradually smeared out and the SL tends to vanish. The reflection pattern transits to a vNMR as seen in Fig. 7.5e–h.

### 7.1.3 *Air/$SF_6$ Interface*

Figure 7.6 shows the interaction from an air/$SF_6$ interface. This is a fast/slow interaction: the sound speed in $SF_6$ is 138 m/s at 293 K. A ring shaped test section was installed in the 60 mm × 150 mm conventional shock tube. The interface tightly sealed with a 30 μm Mylar membrane was rotating at any angle ranging from 0° to 90°. Figure 7.7 show the evolution of shock wave propagating along the interface varying the inclination angle for Ms = 1.40 at 286.7 K. In Fig. 7.7b–d, the initial reflected shock pattern was a SMR and at the critical transition angle of 34°, the transition to a RR occurs. In Fig. 7.7e, f, a SuRR were observed.

## 7.2 Shock Wave Interaction with a Helium Column

Figure 7.8 shows an experimental arrangement of the shock wave interaction with a soap column containing helium. In order to accommodate a vertical helium soap column, the 60 mm × 150 mm diaphragm-less shock tube was turned 90° sideway converting the 150 mm × 60 mm shock tube. The height of the soap bubble column was 60 mm and its diameter was 50 mm; it was stretched between the two walls of the test section by thin brass rings 4 mm in thick and 4 mm in width glued on the upper and bottom walls. Then, the soap bubble column was held vertically for a few minutes being blown by 1015.2 hPa high pressure helium (Nagoya 1995).

To visualize shock waves in the helium soap columns, the collimated object beam *OB* passed the test section from its top to bottom and then reflected from a plane mirror placed at the bottom of the test section. The reflected *OB* passed the

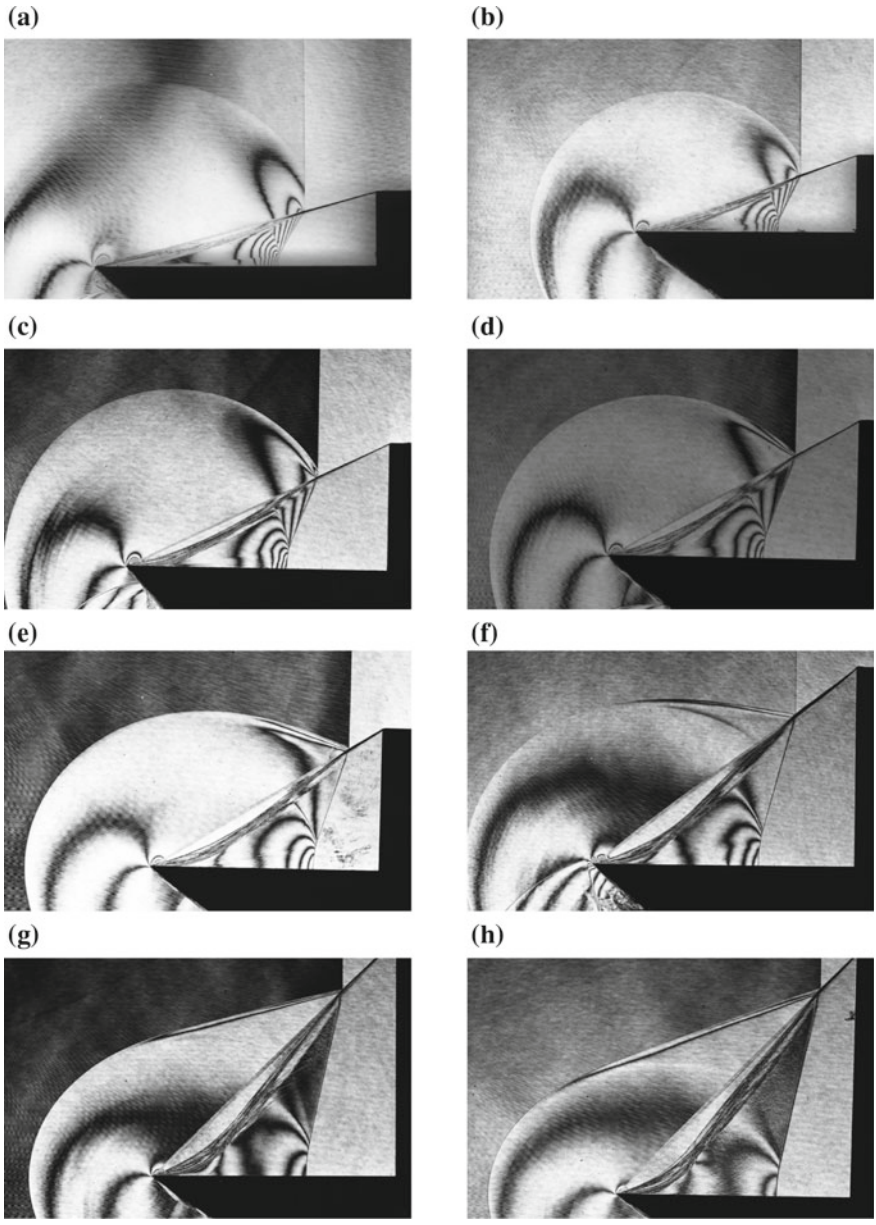


**Fig. 7.5** Shock wave interaction with air/$CO_2$ interface for Ms = 1.20 in atmospheric air at 296.6 K, $CO_2$ exchange time of 10 min: **a** #9306102, Ms = 1.198, $\theta_w = 15°$; **b** #9306101, Ms = 1.201, $\theta_w = 20°$; **c** #9306103, Ms = 1.197, $\theta_w = 25°$; **d** #9306104, Ms = 1.200, $\theta_w = 30°$; **e** #9306105, Ms = 1.200, $\theta_w = 35°$; **f** #9306106, Ms = 1.198, $\theta_w = 40°$; **g** #9306108, Ms = 1.199, $\theta_w = 50°$; **h** #9306109, Ms = 1.199, $\theta_w = 55°$

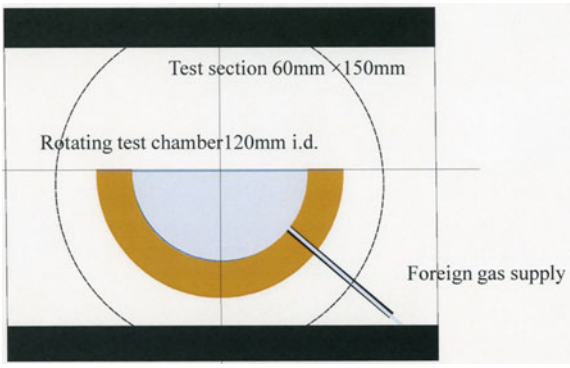


**Fig. 7.6** Test section of air/$SF_6$ interface

test section again, then reflected from a half mirror located in the middle position of the collimated light path and illuminated the holographic film. Hence the *OB* passed the test section twice. With such a double path arrangement, even the 60 mm test section length was doubled. This optical arrangement is illustrated subsequently in Fig. 7.30b.

Figure 7.9 show sequential interferograms of shock/helium column interaction with helium filled soap bubble for Ms = 1.20 in atmospheric air at 295.7 K. A weak transmitted shock wave and a reflected shock wave propagated inside the bubble. The observed sequence of the interaction is very different from the interaction with a rigid cylinder. In Fig. 7.9c, the column started to contract. The transmitted shock wave in helium propagated faster than the IS in air and was released into air ahead of the IS. At the same time, the transmitted shock wave was reflected from the concave interface and focused: see in Fig. 7.9d–i. The patterns of focusing were similar to those observed during the focusing from concave rigid walls. Such effects were caused by the reflection from thin brass rings attached on the upper and lower walls. At the same time, the frontal surface of the column was deformed in Fig. 7.9e and the deformation was promoted.

The IS was diffracted along the rear part of the interface. At the same time, the transmitted shock wave came out from the interface as seen in Fig. 7.9d. The diffracting shock wave and transmitted shock wave interacted at the rear side of the interface in Fig. 7.9g. But such interaction patterns never occurred over a rigid cylinder.

At the same time, the deformed helium column moved to downstream at almost equal to the particle velocity behind the IS. The frontal side of the helium column was gradually flattened as shown in Fig. 7.9m. The deformation was accelerated and eventually became concave as shown in Fig. 7.9m, n. At this stage on, the interval of the double exposure was set to be 600 μs. In Fig. 7.9n, the first exposure was conducted at the moment when the IS arrived at the helium column and the second exposure was conducted when the transmitted shock wave reached at the right hand side of the observed field of view. Hence, the fringes in this interferogram correspond to the difference in the phase angles occurred during these time

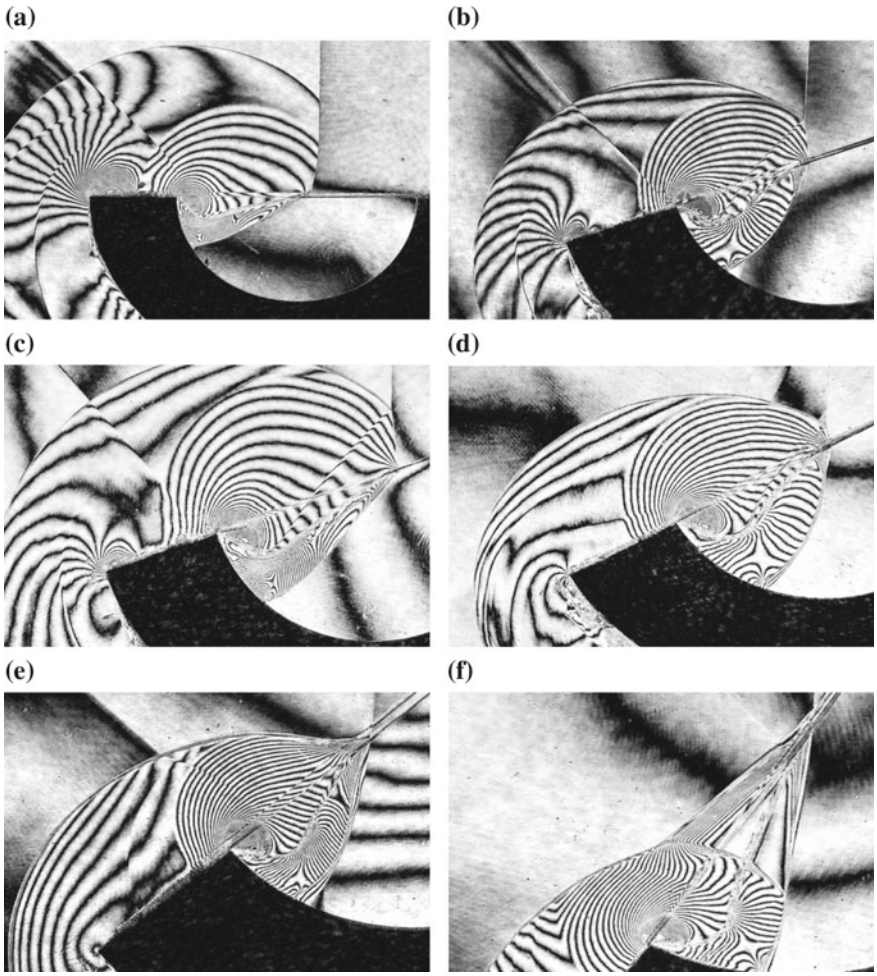


**Fig. 7.7** Shock wave interaction with air/$SF_6$ interface, for Ms = 1.40 in atmospheric air at 286.7 K, Exchange time duration 10 min: **a** #90012308, Ms = 1.722, $\theta_w = 0°$; **b** #90012403, Ms = 1.443, $\theta_w = 20°$; **c** #90012401, Ms = 1.497, $\theta_w = 20°$; **d** #90012406, Ms = 1.380, $\theta_w = 30°$; **e** 90012404, Ms = 1.460, $\theta_w = 40°$; **f** #90012405, Ms = 1.480, $\theta_w = 60°$

intervals. Figure 7.9s shows a single exposure interferogram of the deformation of the helium column. Fringes describing the interfaces were jaggedly shaped, because the fringes were formed by the observation of three-dimensional phenomena with two-dimensional collimated *OB*.

Figure 7.10 show sequential deformations of the helium column at a later stage. With elapsed time, the helium column was deformed like the cross section of mushroom. The helium column moved at almost equal to the particle velocity behind the shock wave. Jaggedly shaped fringes never represented the

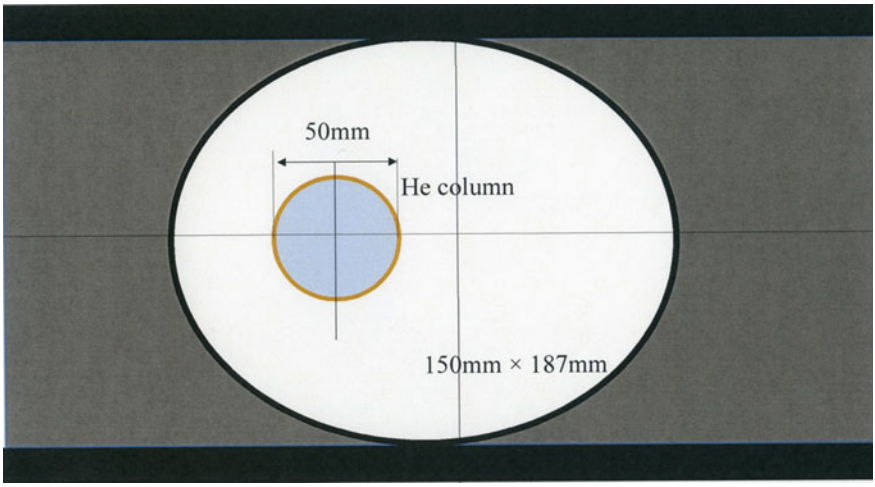


**Fig. 7.8** A soap bubble column of 50 mm in diameter and 60 mm in height was installed horizontally in the 150 mm × 60 mm shock tube. The field of view had an elliptic shape of 150 mm × 187 mm (Nagoya 1995)

two-dimensionally deformation but the integration of the three-dimensional density distribution along the z-direction. The interfacial instability was described by the analytical model of the so-called Richtmyer-Meshkov Instability (RMI) (Nagoya 1995). Analytical description of the RMI was based on the theoretical background of the three-dimensional interaction between the density gradient and the pressure gradient. The RMI was induced in the interaction between the pressure jump across the shock waves and the density jump across the gaseous interfaces. As a result of RMI, three-dimensional disturbances developed and eventually the vortices were formed.

**Fig. 7.9** Sequential observation of shock wave interaction with a helium column for Ms = 1.20 in ▶ atmospheric air at 295.7 K, He bubble 1015.2 hPa: **a** #93120801, 360 μs; **b** #93120701, 375 μs elapsed time from shock wave arrival at the frontal stagnation of the column, Ms = 1.200; **c** #93120811, 415 μs, Ms = 1.215; **d** #93120604, 430 μs, Ms = 1.197; **e** #93120602, 440 μs, Ms = 1.196; **f** #93120606, 410 μs, Ms = 1.196; **g** #93120806, 445 μs, Ms = 1.212; **h** #93120509, 450 μs, Ms = 1.209; **i** #93120607, 460 μs, Ms = 1.195; **j** #93120608, 470 μs, Ms = 1.204; **k** #93120609, 480 μs, Ms = 1.208; **l** #93120802, 500 μs, Ms = 1.206; **m** #93120803, 550 μs, Ms = 1.198; **n** #93120902, 650 μs, Ms = 1.204; **o** #93120903, 700 μs, Ms = 1.206; **p** #93120904, 750 μs, Ms = 1.211; **q** #93120905, 800 μs, Ms = 1.212; **r** #93120908, 950 μs, Ms = 1.208; **s** #93121004, 1.1 ms, Ms = 1.212 single exposure; **t** #93121106, 1.05 ms, Ms = 1.208

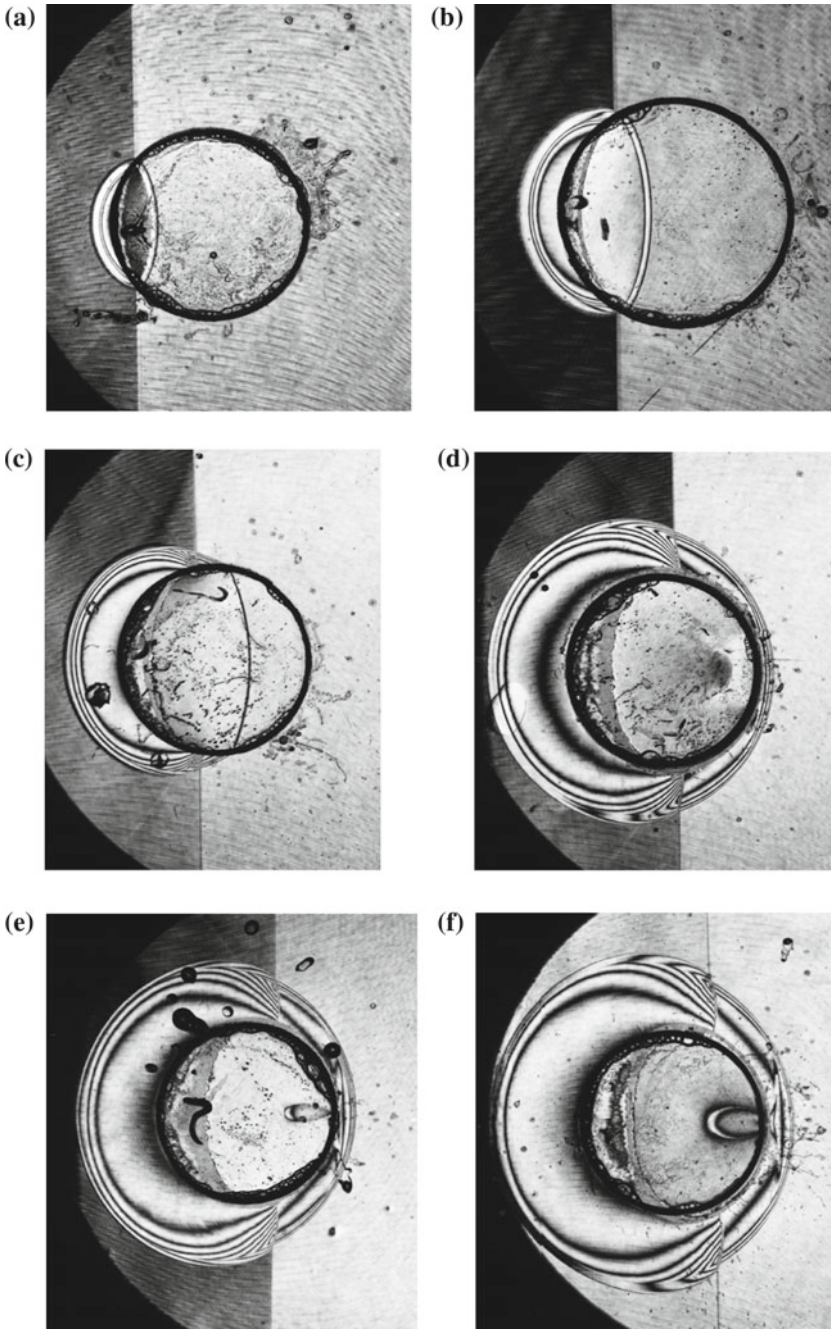
(a)
(b)
(c)
(d)
(e)
(f)

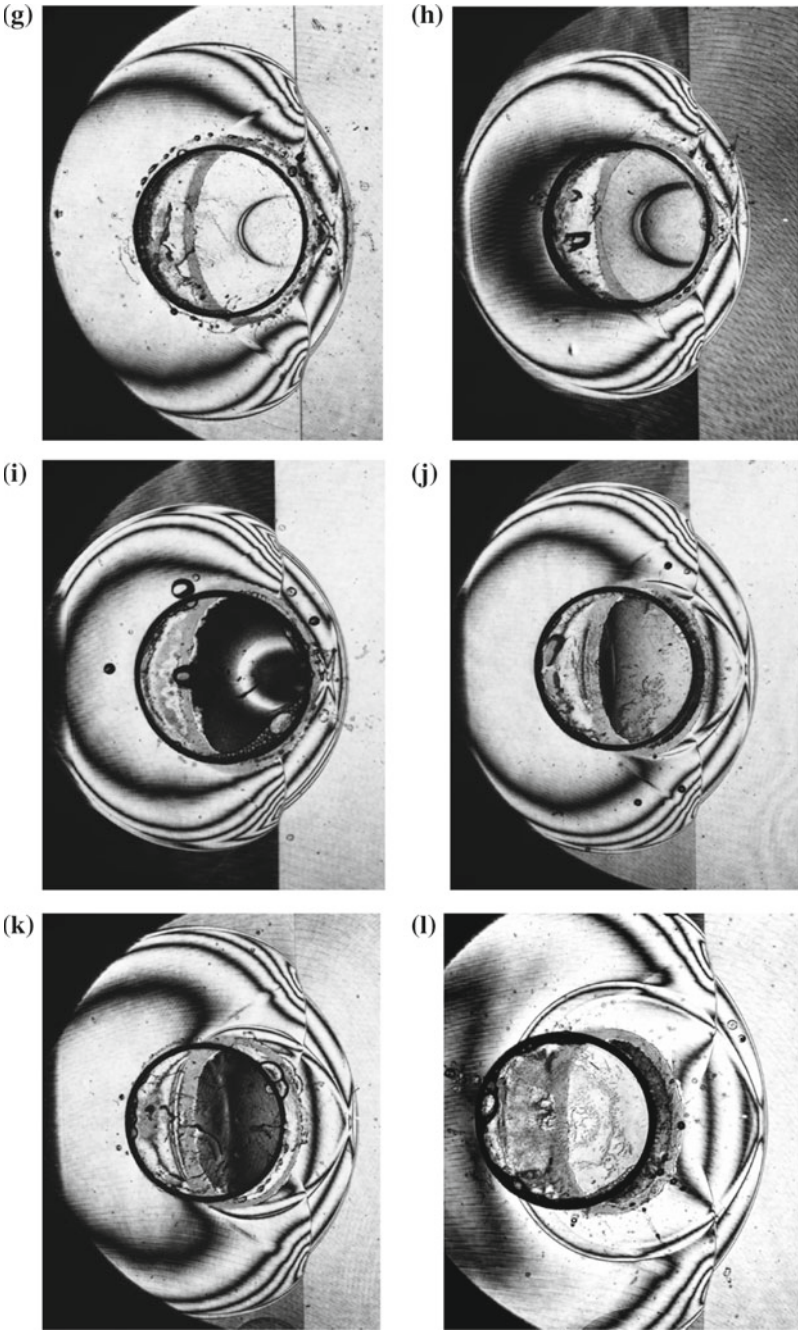


**Fig. 7.9** (continued)

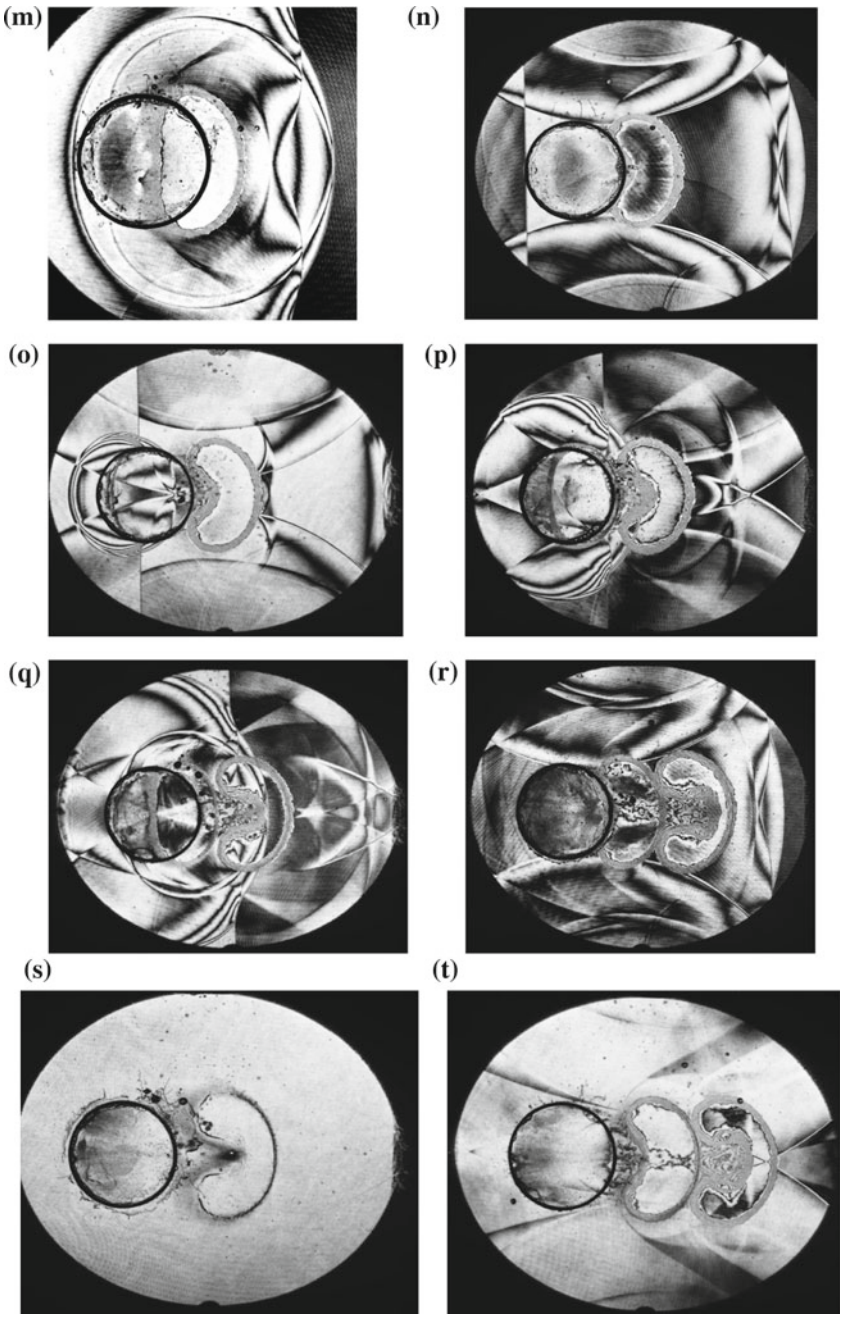


**Fig. 7.9** (continued)

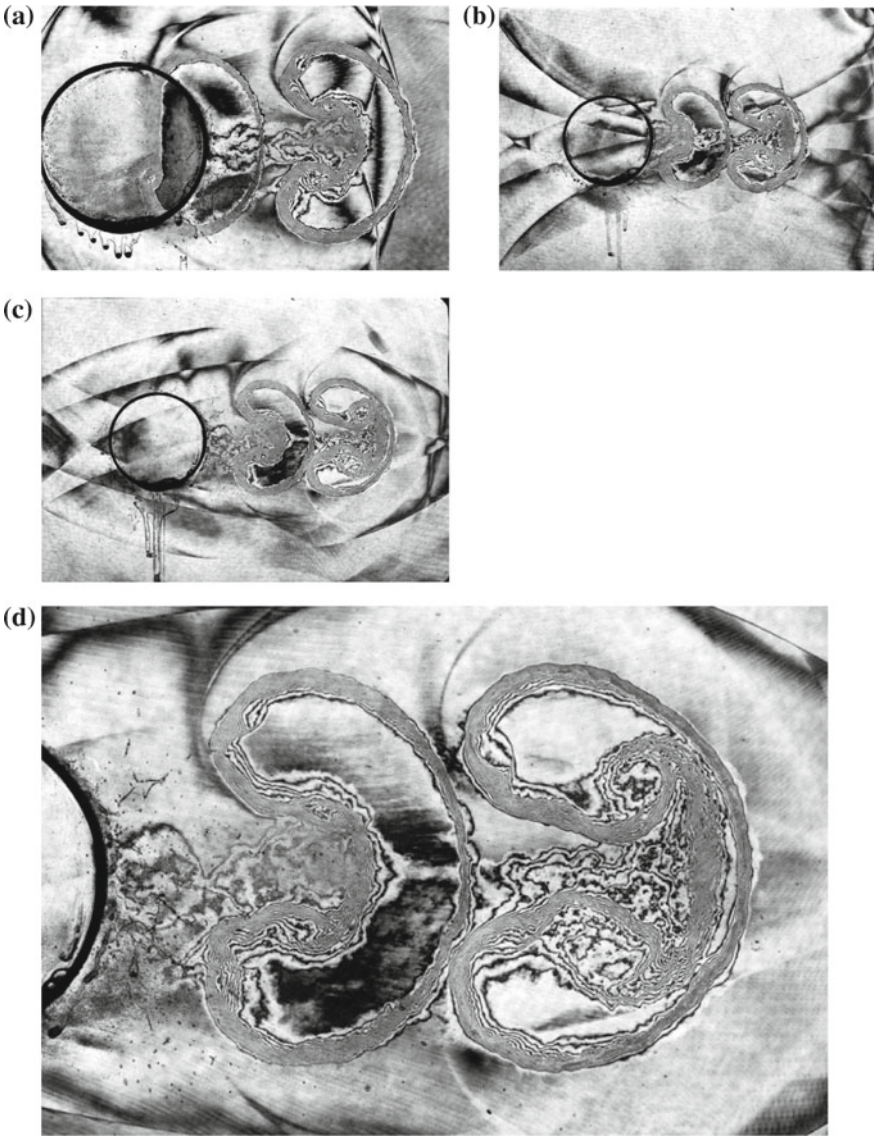


**Fig. 7.10** Later stage of shock wave interaction with a helium column for Ms = 1.21 in atmospheric air at 295.0 K He bubble 1015.2 hPa, the interval of double exposures was 600 μs: **a** #93061106, 1.0 ms from arrival of IS at the helium column; **b** #93061108, 1.2 ms; **c** #93061109, 1.3 ms; **d** enlargement of (**c**)

Figure 7.11 summarizes the positions of helium columns observed in Figs. 7.9 and 7.10. The ordinate denotes the elapsed time in μs and the abscissa denotes the position of deforming helium columns in mm. The distance between the front side

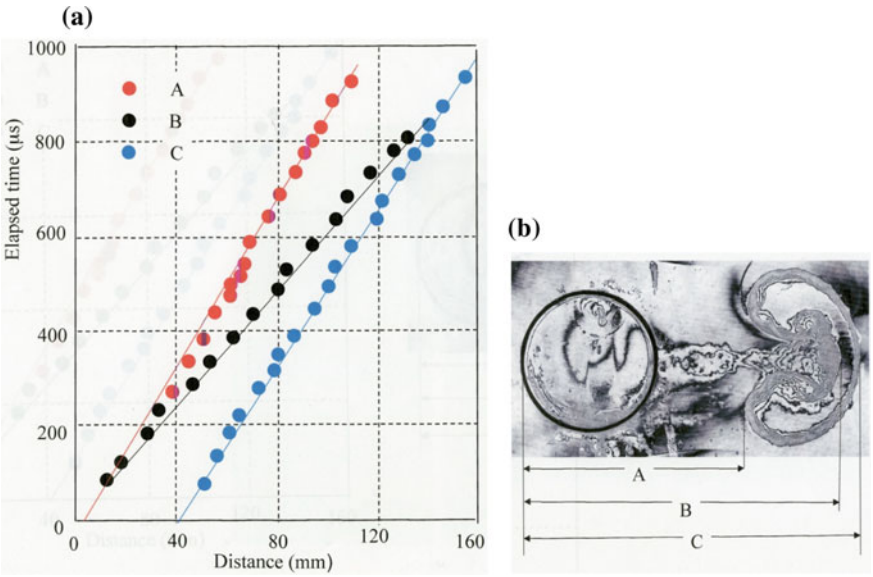


**Fig. 7.11** The motion of helium columns, the summary of Figs. 7.9 and 7.10 (Nagoya 1995)

and the rear side of the helium columns seen in the pictures was almost unchanged and moved at the speed close to the particle velocity behind the IS, whereas the front side of the helium column is accelerated and eventually a mushroom shape of deformation was built up.

### *7.2.1 Side View of a Helium Column*

The impingement of shock waves on the helium column was visualized from the top as seen in Fig. 7.10. Jaggedly observed fringes never meant the two-dimensional interfacial instability but a simple sequence of the integration of three-dimensional density fluctuations conducted along the interface. Therefore, the observation from the side of helium columns would be physically meaningful. Figure 7.12 shows a schematic observation from the side. The helium soap column is supported by thin brass rings from the upper and bottom walls and the IS is impinged from the left. Figure 7.13a shows the helium column prior to the shock wave arrival. Figure 7.13b shows a side view corresponding to Fig. 7.9o. Small protrusions and dents are distributed along the rear side of the column. These are vortices originated as a result of RMI. Straight and parallel fringes on the left correspond to the undisturbed helium column taken at the first exposure. Straight and parallel fringes on the right correspond to the transmitted shock wave visualized at the second exposure. It is emphasized again that the interfacial instability is

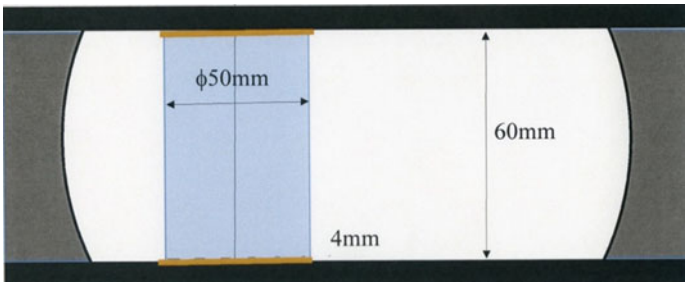


**Fig. 7.12** Experimental arrangement for observing side view of the helium column

not two-dimensional but the three-dimensional which generated vortices. Figure 7.13c corresponds to an earlier stage of the interface deformation corresponding to Fig. 7.9l. Figure 7.13d was taken at 1.0 ms after the arrival of the shock wave at the leading edge of the helium column (Nagoya 1995).

## 7.3 Shock Wave Propagation Over Liquid Surface

### *7.3.1 Air/Silicone-Oil Interfaces*

A 4 m long and 30 mm × 40 mm conventional shock tube made of extruded brass was connected to a 30 mm × 240 mm circular stainless steel test section and already used in the water wedge experiments. Figure 7.14 shows a direct shadowgram of air/silicone oil experiments. Silicone oil (Toshiba Silicone 10cSt) was filled in the hemi-circular space in the bottom and the shock wave propagates in air at supersonic speed in terms of the sound speed in silicone oil (Takayama et al. 1982). The IS was diffracted at the entrance and the transmitted shock wave was reflected from the silicone oil surface. The pattern of the reflected shock wave in air was DMR. The secondary triple point and the resulting Mach stem are clearly visible. When this photograph was taken, these wave patterns were mysterious. The shock wave propagated for Ms = 3.225 at the speed of 1.112 km/s. This is locally supersonic in silicone oil. Its Mach number is M = 1.13, relative to the sound speed in silicon oil. Then the shock wave in the silicone oil looks straight.

Figure 7.15 shows a sketch of the 40 mm deep and 150 mm long hem-circular test piece inserted in the lower part of the 30 mm × 240 mm circular test section. Silicone-oil (Toshiba Silicone 10cSt) was filled in the cavity.

Experiments were conducted for Ms ranging from 2.9 to 3.3 relative to shock wave speed ranging from 900 to 1100 m/s. Figure 7.16 shows shock waves propagating over the air/silicone-oil interface at variable Ms. When the incident shock wave speed, $u_s$, is lower than the sound speed in silicone oil, $a_{silicon}$,

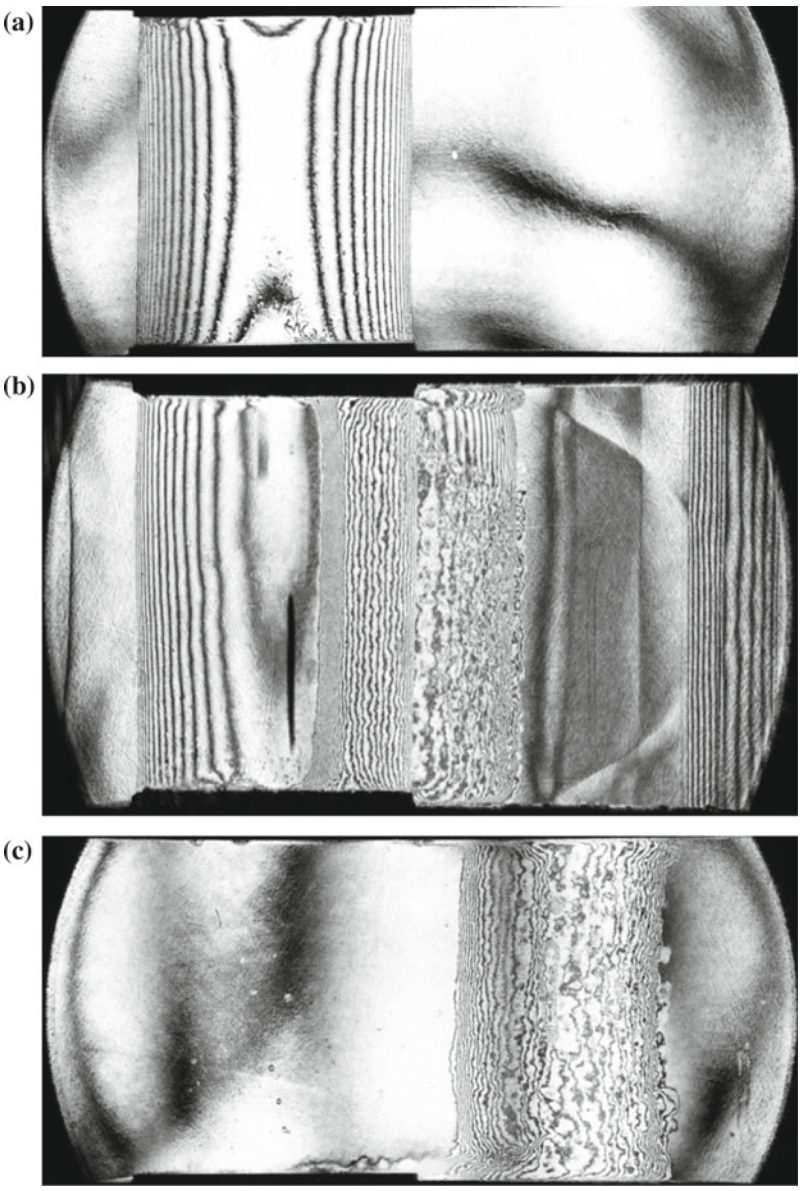


**Fig. 7.13** Observation from side for Ms = 1.20 in air at 1013 hPa, 295 K, helium pressure at 1015.2 hPa: **a** #93112302, before shock loading; **b** #93111813, 500 μs after arrival of the shock wave at the column, Ms = 1.20 at 1015.2 hPa; **c** #93112211, 900 μs, Ms = 1.19; **d** #93112310, 1.0 ms, Ms = 1.21

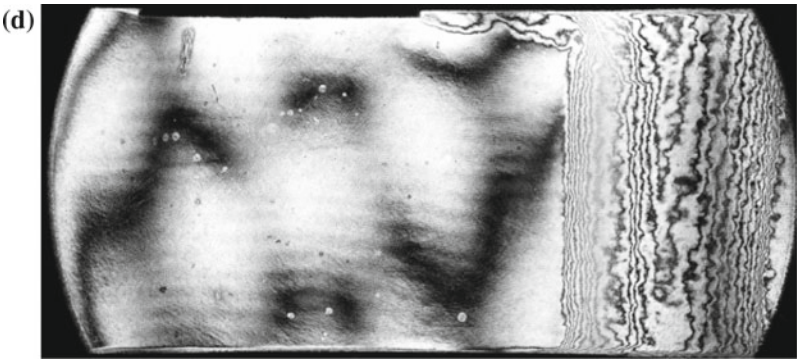


**Fig. 7.13** (continued)

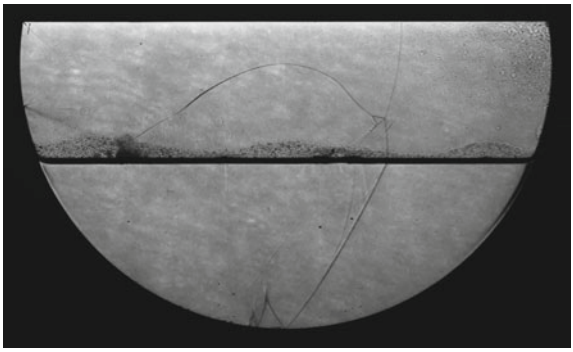

**Fig. 7.14** Shock wave propagation along an air/silicone oil interface: Direct shadowgraph, #75050510, Ms = 3.225 in air at 150 hPa

$u_s < a_{silicon}$, compression wavelets are generated in the silicone oil and propagate at $a_{silicon}$. At $u_s \approx a_{silicon}$, the compression wave coalesced into a weak shock wave.

Figure 7.16 shows sequentially transmission of a shock wave at sonic speed $u_s = a_{silicon}$ in silicone oil. The shock wave in air and the transmitted wave in silicone wave are normal to the interface. For $u_s > a_{silicon}$, an oblique shock wave appears with an inclination angle θ, where $\sin\theta = a_{silicon}/u_s$, whereas $u_s < a_{silicon}$ the sonic wave propagates in silicone oil ahead of the shock wave in air.

As $a_{silicon}$, is 985 m/s at 290 K, the transmitted wave pattern inside silicone-oil varied depending their speeds. Figure 7.17 summarize the results. In Fig. 7.17a, b, c, the shock speed is subsonic $u_s < a_{silicone}$. The wave in silicone oil is visible in front of the shock wave in air. In Fig. 7.17d the shock wave in air propagates at almost the sonic speed in silicone oil and then it appears to be normal to the silicone oil surface $u_s \approx a_{silicon}$. In Fig. 7.17e–g, the shock wave in air propagates at supersonic speed $u_s > a_{silicone}$. Then shock wave in silicone oil appear to be oblique to the silicone oil surface.

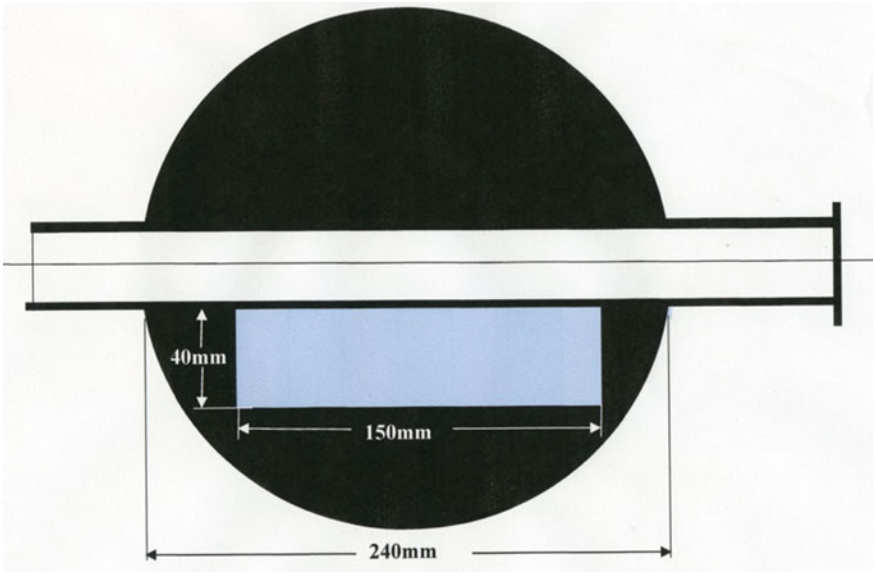


**Fig. 7.15** Sketch of the test section: shock propagation along silicone oil surface (Takayama et al. 1982)

## 7.4 Shock Waves Induced by the Injection of High-Speed Jets

High speed water jets in air are often accompanied by high frequency noises when the jet speeds exceed the sound speed in air. To conduct analogue experiments of diesel fuel injections of a 7 mm bore compact gun was constructed in which the energy sources were convertible from gas gun to powder gun. In the gas gun mode operation, high pressure gas was used and in the powder gun mode operation, smokeless powder was used. The compact gun has a 7 mm bore and 10 mm long and can launch a 1.0 g weight high density poly-ethylene piston at muzzle speeds ranging from 0.1 to 1 km/s. The double exposure holographic interferometry was intensively used for visualization (Shi 1995).

Figure 7.18 show high speed liquid jets and shock waves induced in front of the jets. In Fig. 7.18a, b kerosene and water jets were ejected through a 0.5 mm diameter nozzle attached to a storage chamber of the gas gun, respectively. Grey shadows show the liquid jet boundary forming very irregular shape, whereas bow shock waves were formed smoothly at the head of liquid jets, respectively. In Fig. 7.18c–e, diesel fuel ejections through with a 0.5 mm diameter 90° two-hole nozzles were sequentially observed. Bow shock waves were formed ahead of impulsively ejected diesel fuel jets.

Figure 7.18 show bow shock waves formed in front of the jets and oblique shock waves were intermittently generated along jagged shaped jet boundary. The

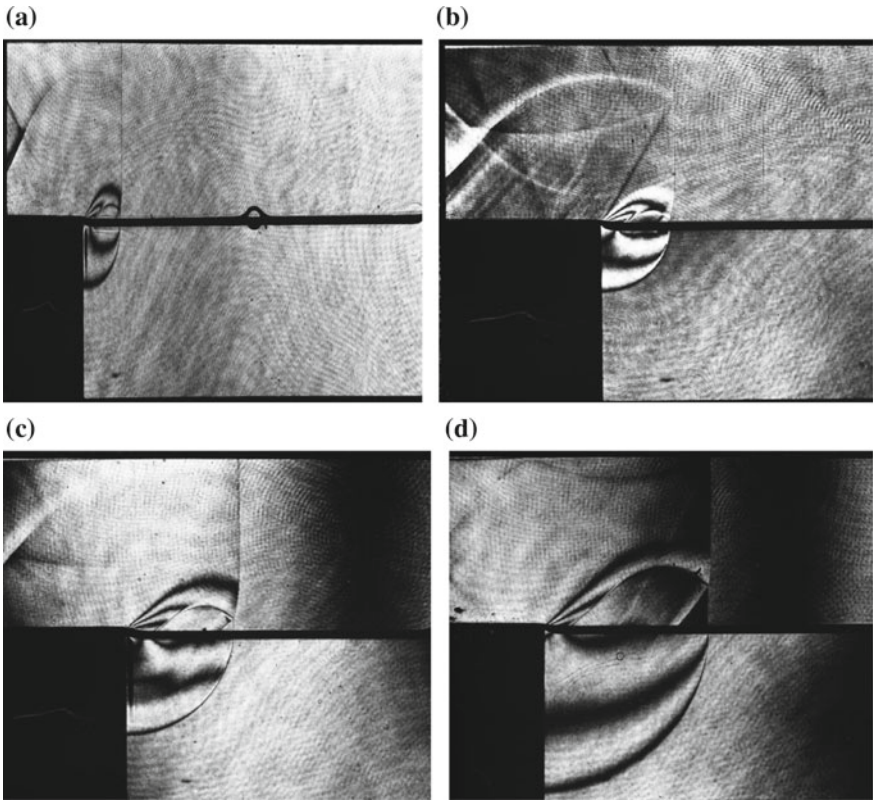


**Fig. 7.16** Sequential observations of shock waves at sonic speed, $a_{silicon} = u_s$, Ms = 2.80 ± 0.05 in air at 125 hPa, 295 K: **a** #81052601, 8 μs from the entrance corner; **b** #81052202, 16 μs from the entrance corner; **c** #81052202, 22 μs from the entrance corner; **d** #81052605, 40 μs

irregularly shaped boundary was induced by not only turbulent mixing over the jet boundary and also by inherited intermittent stress wave propagation inside the titanium container that occurred when the projectile impacted the gun. The titanium container was not a rigid body but was deformed by the propagation of longitudinal and transversal waves upon the piston impingement. A 15 mm diameter powder gun was constructed and launched a 15 mm diameter and 25 mm long high-density polyethylene projectile weighing 4 g at a muzzle speed of 1.8 km/s and eventually achieved approximately 4 GPa in diesel fuel and water stored in a few $cm^3$ titanium container positioned at the end of the launch tube. In discharging the test liquid through a 0.5 mm diameter nozzle, the jet speed of approximately 3.0 km/s was readily obtained. In Fig. 7.18f–h, bow shock waves were formed in front of the jets and oblique shock waves were intermittently generated along jaggedly shaped jet boundary. Even though the edges of the jets looked very irregular, the shock waves looked smooth because the waves are formed from accumulation of disturbances

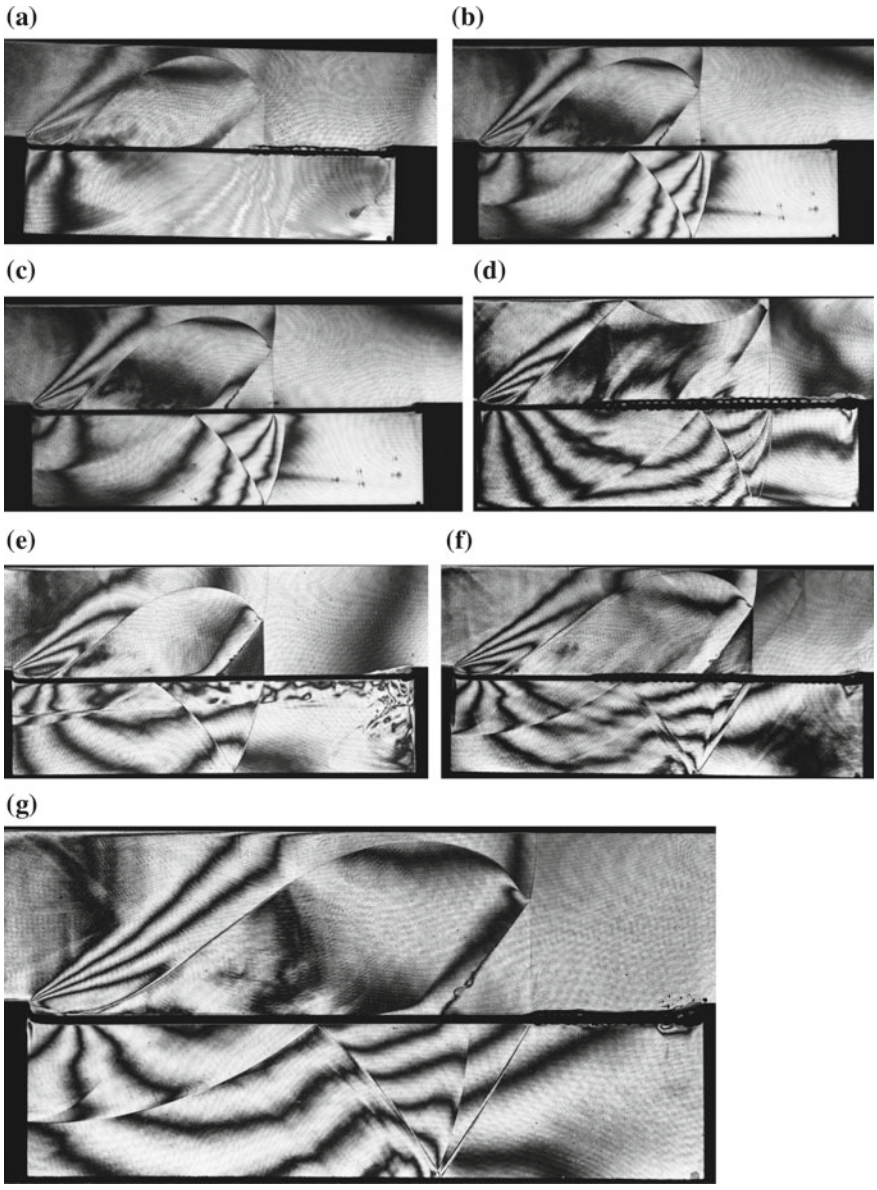


**Fig. 7.17** Shock wave propagation over silicone oil: **a** #81020602, Ms = 3222, $u_s > a_{silicon}$; **b** #81020613, Ms = 3.016, $u_s$ 0< $a_{silicon}$; **c** #81012901, Ms = 2.946, $u_s < a_{silicon}$; **d** #81012202, Ms = 3.061, $u_s \approx a_{silicone}$; **e** #81020605, Ms = 3.229, $u_s > a_{silicon}$; **f** #81012301, Ms = 3.350, $u_s > a_{silicon}$; **g** #81012302, Ms = 3.367, $u_s > a_{silicone}$

induced by the irregularities. The irregularly shaped boundary was induced due to not only turbulent mixing over the jet boundary but also inherited intermittent stress wave propagation inside the titanium container: These were created by the projectile impact. In Fig. 7.18h, the leading edge of the jet was not necessarily form a smooth blunt shape but became a jagged shape. Hence the shape of shock wave generated in front of the jet also took irregular shapes. The titanium container was not a rigid body but was readily deformed by the propagation of longitudinal and transversal waves induced by the piston impingement.

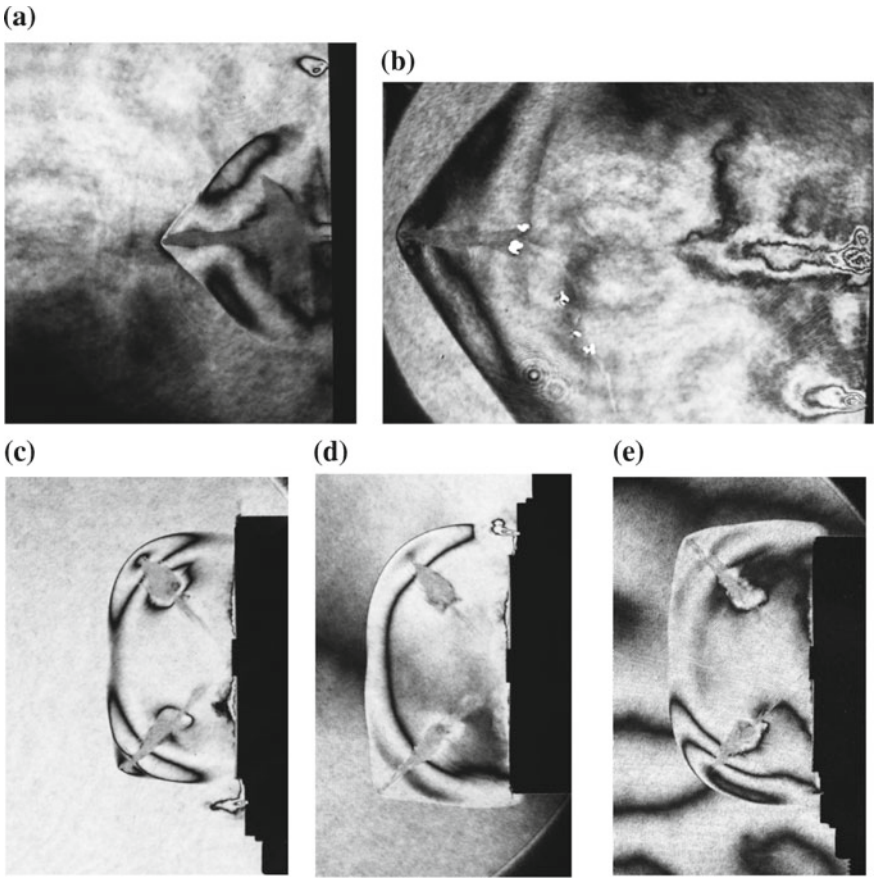


**Fig. 7.18** Shock wave induced by high speed jet: **a** #92040603, injection pressure 12.3 atm, jet speed 480 m/s, fuel kerosene, nozzle diameter 0.5 mm; **b** #92040802, water jet, injection pressure 14.4 atm, nozzle diameter 0.5 mm; **c** #93032010, two-hole $\theta = 90°$ nozzle diameter 0.5 mm, diesel fuel, injection pressure 13.5 atm; **d** #93032011, two-hole $\theta = 90°$ nozzle diameter 0.5 mm, diesel fuel, injection pressure 13.5 atm; **e** #93032201, two-hole $\theta = 90°$ nozzle diameter 0.5 mm, diesel fuel, injection pressure 12.6 atm; **f** #94060303, nozzle diameter 2.5 mm, water jet driven by burning smokeless powder weighing 2 g; **g** #94060304, nozzle diameter 2.5 mm, water jet driven by smokeless powder 2 g; **h** #9406080, nozzle diameter 0.6 mm, light oil jet driven by smokeless powder 4 g

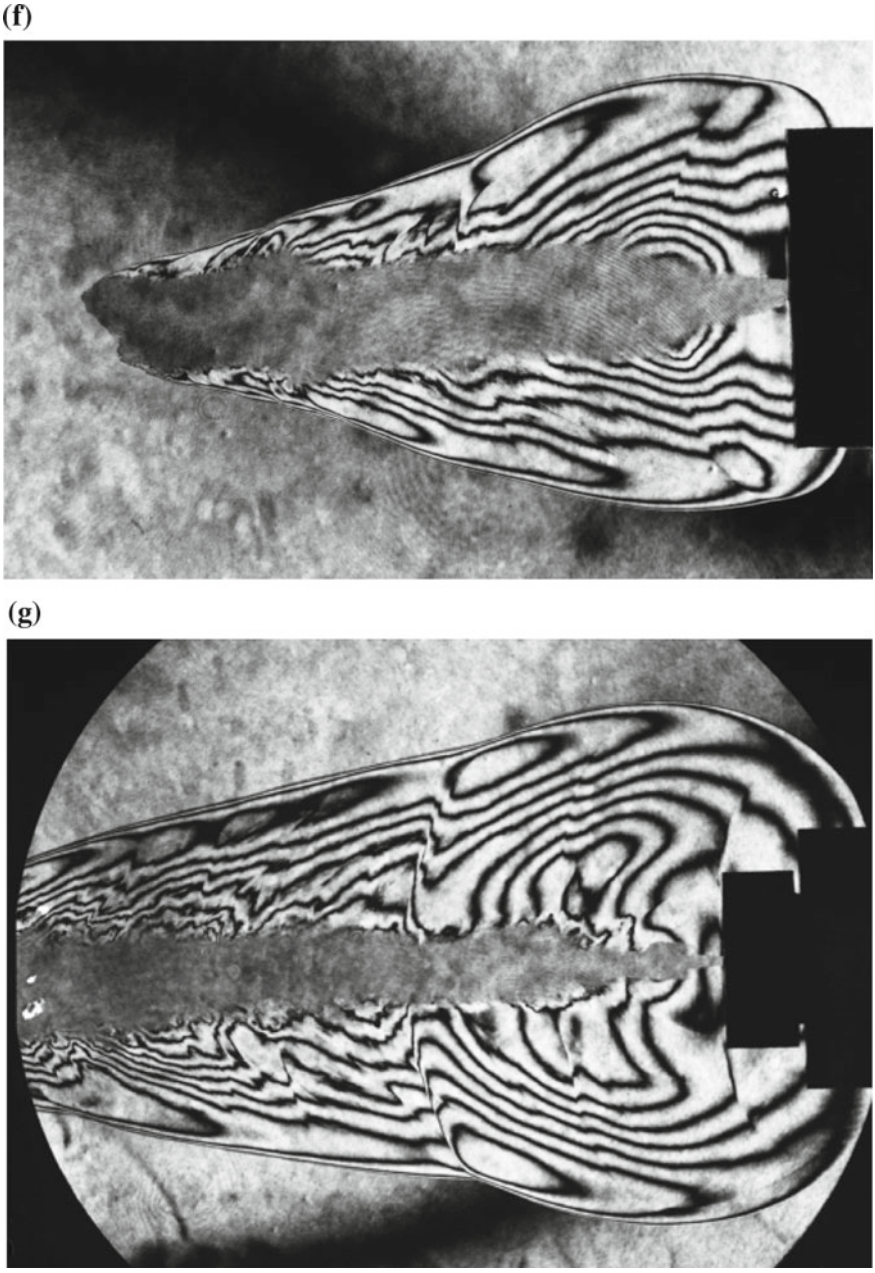


**Fig. 7.18** (continued)

(h)

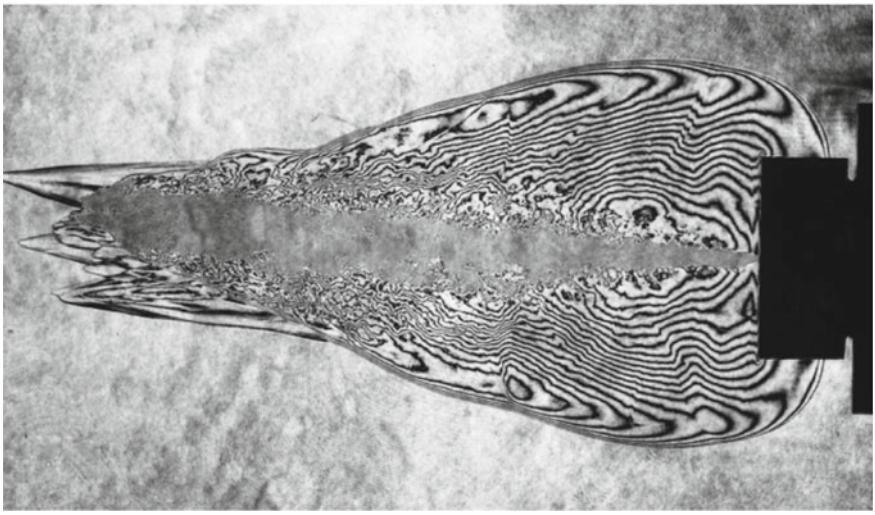

**Fig. 7.18** (continued)

### 7.4.1 *High-Speed Liquid Jet Induced by a Two-Stage Gas Gun*

Pianthong (2002) worked on high-speed jet formation using a compact powder gun (Shi 1995) and measured the effect of stress wave propagations in the powder gun on the jet formation. Matthujack (2000) constructed a vertical two-stage gas gun and revealed that the irregular jet shapes were caused by the stress wave propagation in the nozzle. Figure 7.19a shows the two-stage gas gun supported vertically with two pillars. The gun was movable smoothly up and down suspended with linear guides which enabled to conduct fine measurements.

The gun consisted of a co-axially arranged 230 mm diameter and 1.5 m long high pressure chamber and a 50 mm diameter and 2.0 m long pump tube. A 50 mm diameter and 75 mm long high-density polyethylene piston weighing 130 g was accelerated driven by compressed helium filled in the pump tube. Then the resulting high pressure helium projected a 15 mm diameter, 20 mm long and weighing 4.2 g polyethylene projectile downward into an acceleration tube. Figure 7.19b shows the test section. The acceleration tube had 3 mm diameter holes distributed in a line which eliminate a detached shock wave created ahead of the projectile and at the same time worked to split the projectile from the sabot. The projectile hit a nozzle block in which the liquid under study was filled. The jets were ejected from the nozzle int the test section and visualized. Figure 7.19b shows the arrangement for pressure measurement using a fiber optic probe hydrophone.

Figure 7.20a shows a nozzle made of high strength carbon steel in which the test liquid is filled. Upon the impingement, the liquid was spontaneously pressurized

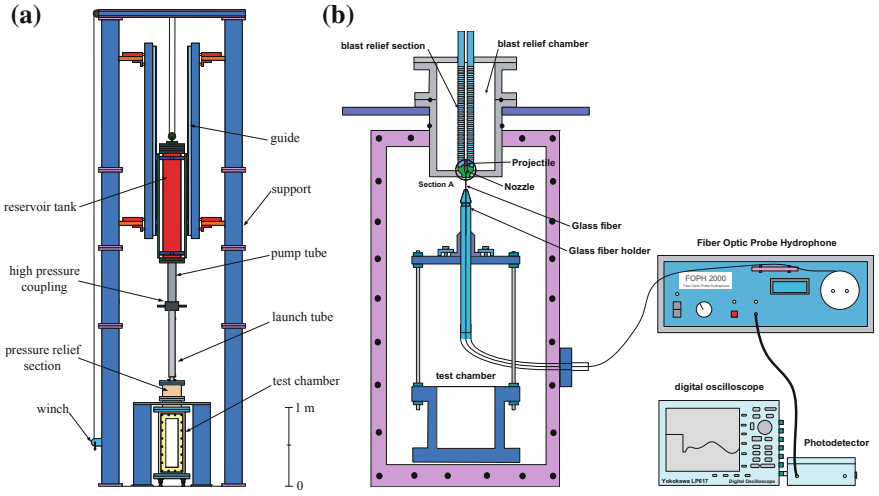


**Fig. 7.19** Experimental setup: **a** gas gun accelerating projectile; **b** installation of the nozzle and pressure transducer (Matthujak 2007)

and ejected. The entire launch tube and the acceleration tube were accommodated in a 305 mm diameter and 850 mm long cylinder and installed in a rectangular observation chamber as shown in Fig. 7.19b. An optical fiber pressure transducer (FOPH2000 RP Acoustic Co. Ltd) was inserted into the exit of the nozzle facing to the liquid jet. The present pressure transducers are not using the piezo effect but detect optically the change in phase angle at the spot in water. The principle is the same as double exposure holographic interferometry. Irradiating the test water with a coherent laser beam through a 0.7 mm diameter optical fiber, the time variation of this laser beam is continuously monitored. This laser light beam is equivalent to the *OB* of the holographic interferometry. The time variation of the *OB* is simultaneously compared with undisturbed source laser beam which is equivalent to the *RB*. Then from the comparison of phase angle variation between the two beams, the density variation is obtained continuously. Trusting the Tait equation (Tait 1888), the density variations are converted readily to the pressure variations. If the equation of state and the relationship of refractive index and density is known for any liquids, this optical pressure transducer can be applied to measure pressure variations in any liquids.

The optical fiber has 0.7 mm diameter and response frequency of 10 MHz and hence this pressure transducer is wonderful for underwater shock wave study at the pressure range below 25 GPa. Figure 7.20b shows the result of the measured stagnation pressure of the jet. The ordinate denotes the stagnation pressure in MPa and the abscissa denotes the elapsed time in μs. Peak pressures A and B correspond to longitudinal and transversal stress waves released from the nozzle into the water. The values of peak pressures A and B are high. However, as these peak pressures were maintained for a very short time, then their values of the impulses are just

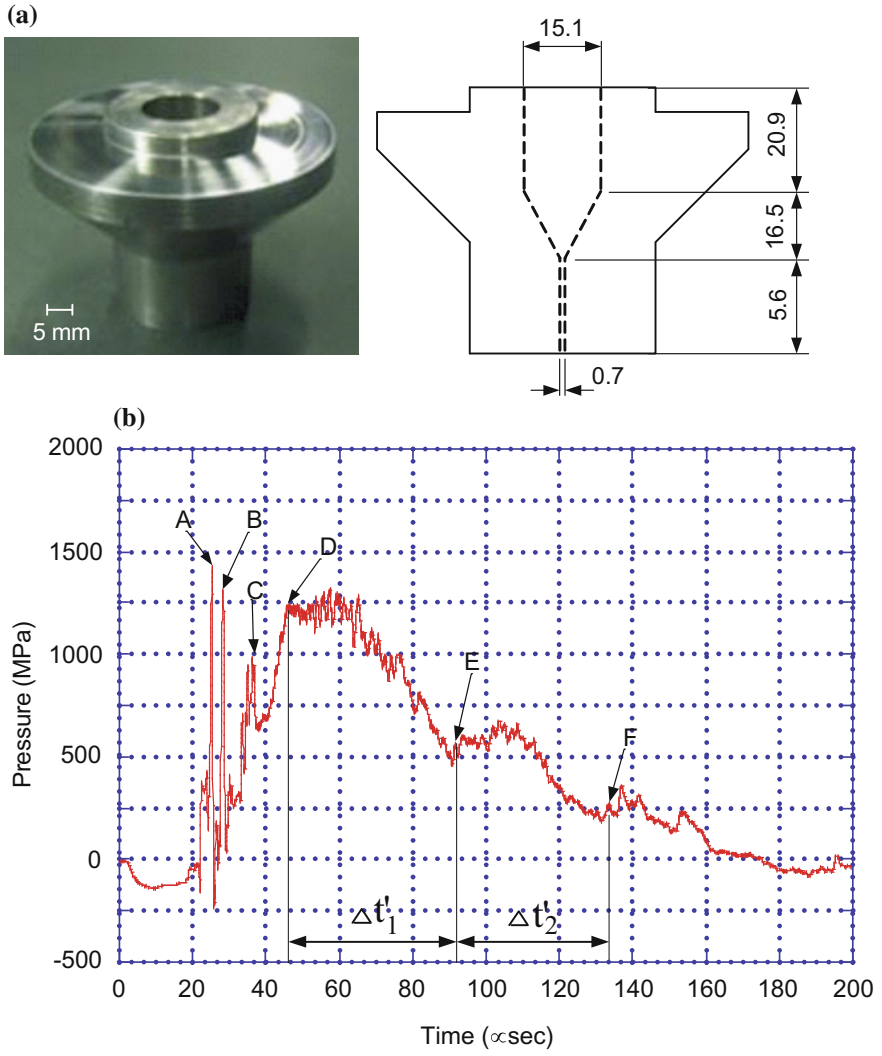


**Fig. 7.20** Pressure measurement: **a** nozzle structure in (mm); **b** the results of pressure measurements (Matthujak 2007)

modest. These intermittent peak pressures D, E, and F correspond to the first, second, and third impulses.

Figure 7.21 summarize jet formation of water, Kerosene, Diesel fuel, and gasoline. The visualizations were conducted using direct shadowgraph and the images were recorded by a high speed video camera Shimadzu SH100 at the framing rate of $10^6$ frame/s. Jets are released from the 0.5 mm diameter nozzle and are the fastest immediately after the ejections. Hence, on the first frames, the

detached shock waves appeared in front of the leading jets. The oblique shock waves appeared from the nodes of the jets and their inclination angles are, so far as estimated from the pictures, range 7°–10°. The jet speed can reach about 2.0–3.0 km/s. With propagation, the inclination angles of the jets increase, which meant the attenuation the jet speeds. As seen in Fig. 7.20b, the peak stagnation pressures in the liquid container decrease intermittently. The intermittent acceleration induced nodes along the jet structure and shock waves are also generated at individual nodes. This sequence promotes the deformation of the jet and also positively contributes to the atomization of fuel jets. The sequence of formation and deformation of high speed jets differ significantly depending on liquid type. This implies the dependence of physical properties determining directly the process of the jet formation. For the jet speed at 2.0 km/s, for example, the stagnation temperature in the shock layer would exceed well over 3000 K. If such a condition is maintained longer duration of time, it would contribute to the atomization of fuel and might have induced auto-ignition. However, it has not happened so far. As seen in Fig. 7.21, the elapsed time of jet formation is at longest 600 μs. This is much shorter than the induction time for auto-ignition.

## 7.5 Shock Wave Interaction with Droplets

Holographic interferometric visualization is one of a useful methods of shock tube experiments. In the 1980 a collaboration started with Dr. T. Yoshida of Tohoku University Faculty of Engineering and visualized droplet shattering upon shock wave loading (Yoshida and Takayama 1985). The collaboration progressed when Dr. A. Wierzba of the Institute of Aviation Warsaw joint the project (Wierzba and Takayama 1987).

### *7.5.1 Shattering of Droplets Falling in a Line by Shock Wave Loading*

When the liquid droplets were exposed suddenly to high speed flows, the droplets shattered. This is one of the fundamental research topics of shock wave research. Droplet breakup is categorized by a dimension-less similarity parameter, the so-called Weber number, We, which is defined as $We = \rho u^2 d/\sigma$ where u, d, ρ, and σ are particle velocity, droplet diameter, liquid density, and surface tension, respectively. The We number is, in other words, a ratio of dynamic energy to the surface tension.

Figure 7.22 shows schematic illustrations of droplet shattering. For a small $We < 14$, a vibrational type breakup occurs. At a larger We, droplets bulge into a bag shape and eventually collapse. Breakup patterns accompanying fragmentation

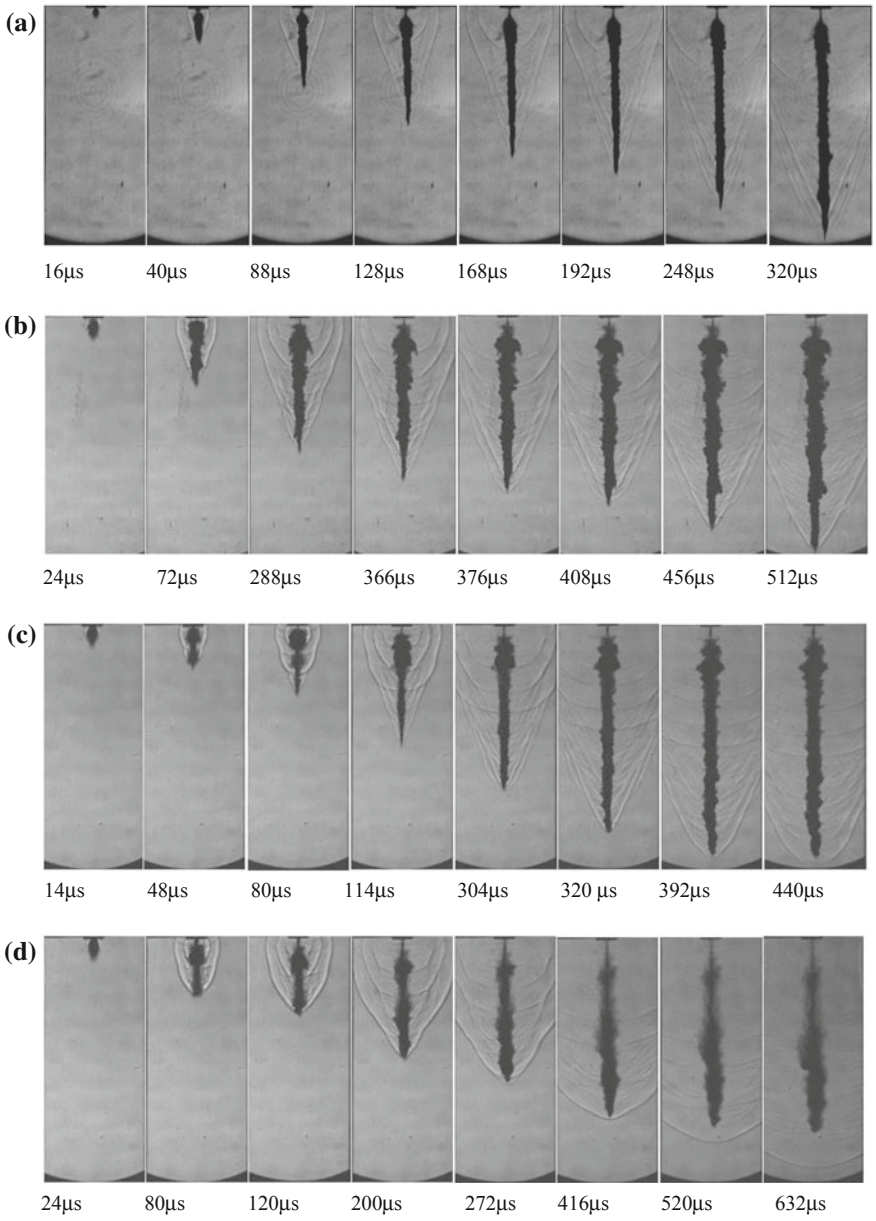


**Fig. 7.21** Evolution of high speed liquid jets: **a** water $V_{piston}$ = 317 m/s; **b** kerosene, $V_{piston}$ = 305 m/s; **c** diesel oil, $V_{piston}$ = 295 m/s; **d** gasoline, $V_{piston}$ = 295 m/s

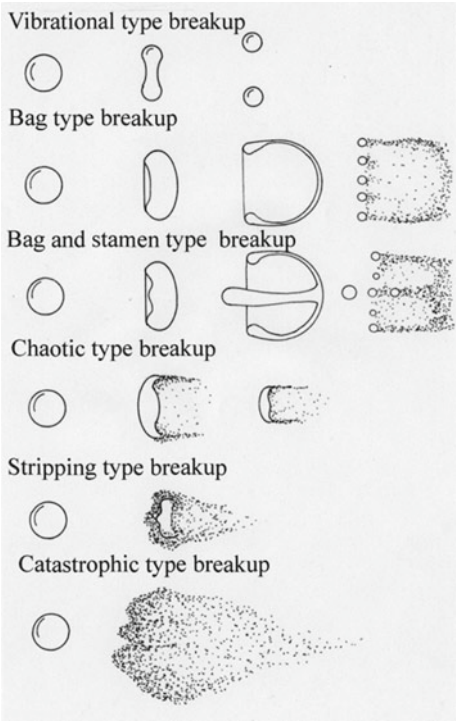


**Fig. 7.22** Different patterns of droplet shattering (Wierzba and Takayama 1987)

the so-called stripping type breakup occurs at about We $\sim$ 2000. For further larger We, a droplet is instantaneously fragmented into mist and hence is named as a catastrophic type breakup. A comprehensive reference survey was reported by Wierzba and Takayama (1987) and Gelfant et al. (2008). Droplet shattering is applied to science, technology, and industry, for example, chemical processes in two-phase flow systems, rain erosions in supersonic flights, spray combustions and many others applications.

Experiments were conducted in the 60 mm $\times$ 150 mm conventional shock tube and the breakup process was observed using double exposure or single exposure holographic interferometry. Test liquids were water and ethyl alcohol which were intermittently dripped from a small hole on the upper wall of the shock tube using an ultrasonic oscillator. Yoshida and Takayama (1985) designed the oscillator. Test liquids were filled in a capillary tube connected to a 0.7 mm diameter nozzle and oscillated at the frequency of 100–200 Hz. The droplet diameter and their interval were adjusted tuning the oscillator's frequency. Figure 7.23 shows an actuator for introducing droplets in a well controlled fashion into the test section. Selecting nozzle shapes and operational conditions, gas filled liquid bubbles of about 4 mm diameter can be introduced to the test section.

The droplets shattering is also conducted in high-speed wind tunnel flows. It was often argued that the droplet shattering in a high-speed wind tunnel flow is

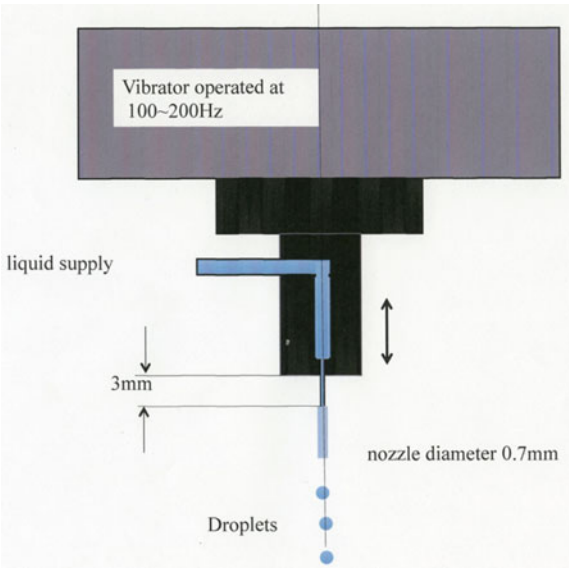


**Fig. 7.23** Actuator for introducing droplets into the test section (Yoshida and Takayama 1985)

conducted in a steady flow, while that in shock tube flows is conducted in an unsteady flow. A question arises that there may be a difference in the shattering processes in the wind tunnel flows and the shock tube flows. However, the droplet shattering in the wind tunnels is not a steady process as the introduction of the droplets into the wind tunnel flows is unsteady. The unsteadiness governs the rest of the shattering procedure. In the shock tube flows, the introduction of the droplets exhibited unsteadiness and it remains until the early wave interaction around the droplets disappears and then the flow became steady for a while. At the later stage, the droplet shattering takes the same procedure appearing in the wind tunnel flows.

Figure 7.24 show a sequential observation of shattering ethyl alcohol droplets of 0.76 mm diameter and that are introduced into the shock tube with separation of about 6–8 mm. The droplets are exposed to interval exposed to a shock wave of Ms = 1.40 and consequently the flow behind the shock wave in atmospheric air at 289.6 K. The liquid jet was oscillated at frequency 144 Hz and became droplets in a line falling into the shock tube. At the earlier stage of the shock wave impingement, the procedure is similar to the shock wave/solid sphere interaction. In Fig. 7.24f, the boundary layer separation promotes the droplet deformation and wakes development. Figure 7.24k shows that the droplet volume increases monotonously with elapsing time. Although wave motions inside the droplet are not observed, transmitted waves and their reflections inside the droplet would promote the deformation process. Reinecke and Waldmann (1975) tried to visualize the droplet deformation by introducing radiography. Holographic interferometry also gave better resolution of images than conventional visualization methods used for estimating the wave motion inside droplets. Advance in numerical simulations someday would reproduce the wave motion inside deforming droplets even in a row.

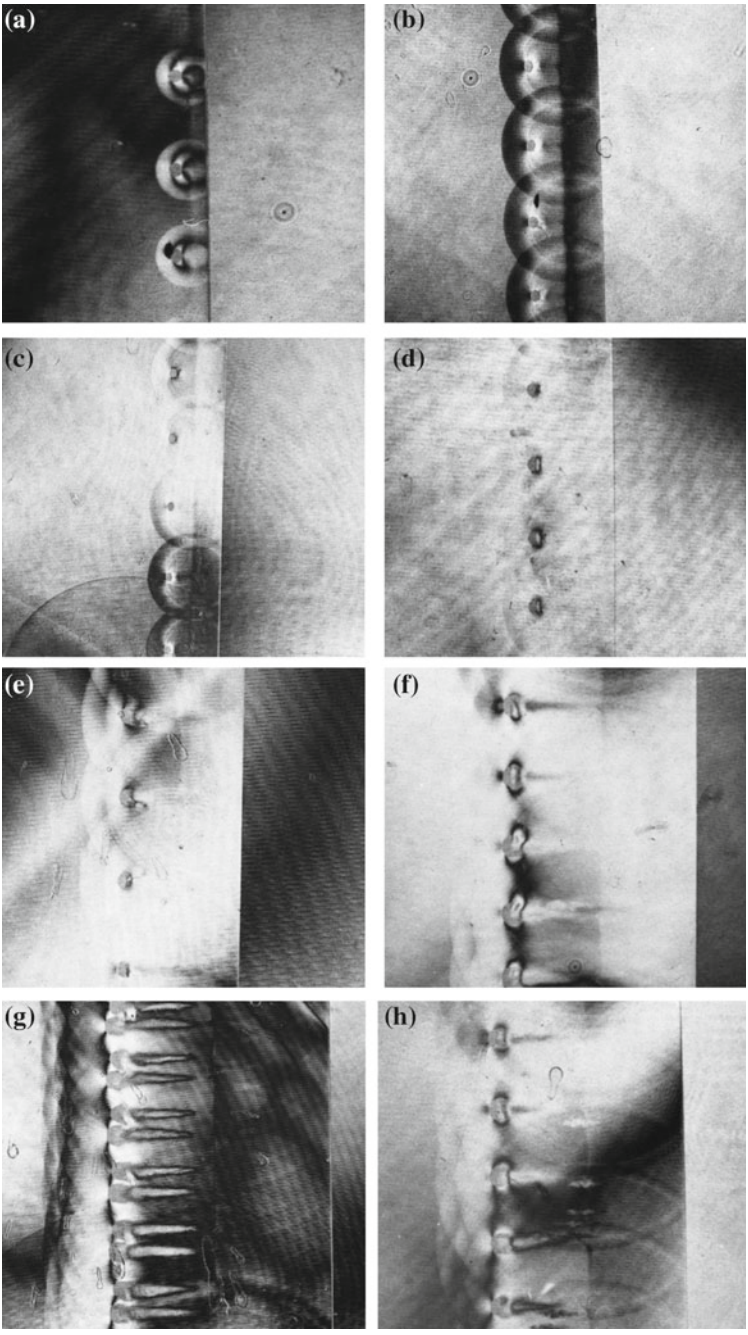


**Fig. 7.24** Shattering of ethyl alcohol droplets of d = 0.76 mm for Ms = 1.601 in atmospheric air at 289.6 K, at frequency f = 144 Hz: **a** #83110707, 450 μs from trigger point; **b** #83111709, 485 μs; **c** #83111705, 490 μs; **d** #83110706, 470 μs; **e** #83111706, 500 μs; **f** #83110704, 490 μs; **g** #83111710, 485 μs; **h** #83110703, 510 μs; **i** #83111708, 520 μs; **j** #83110702, 530 μs; **k** #83110701, 550 μs

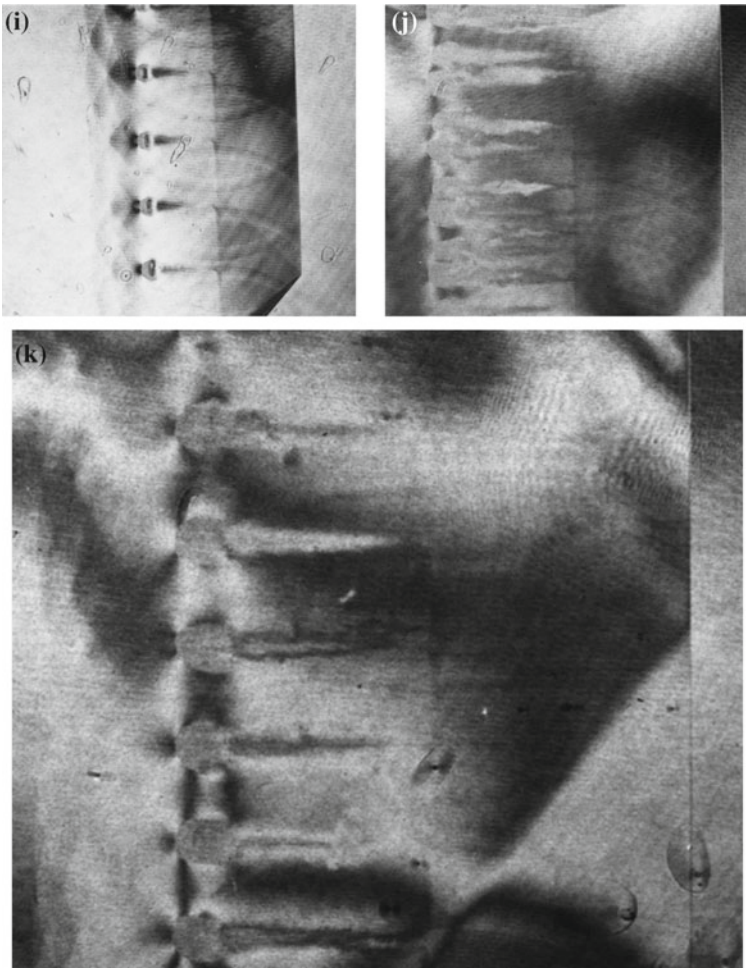


**Fig. 7.24** (continued)

Comparing the background contrast with water droplets seen in Fig. 7.25, a slight deviation of grey contrast is visible between ethyl alcohol droplets and water droplets. Probably the contrast difference indicates change in the rate of evaporation which would decisively affect the refractive index of the gas mixture in vicinity of the droplets. Figure 7.25 show shattering of 1.0 mm diameter water droplets, introduced at space difference of about 5–7 mm and exposed to Ms = 1.58 shock wave in atmospheric air at frequency of 150 Hz. Figure 7.25d shows a single exposure interferogram, which shows a sign of boundary layer separation from the droplet's equator.

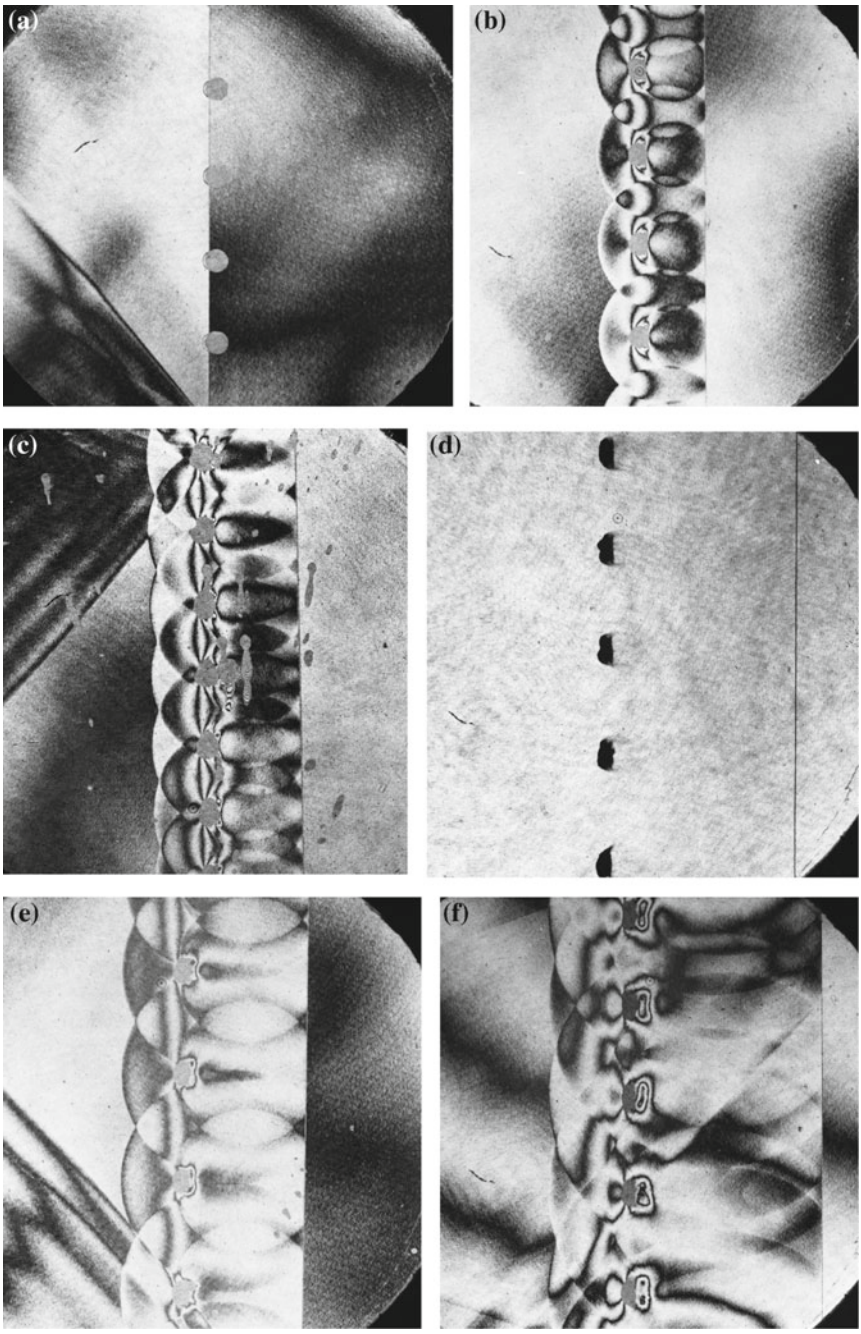


**Fig. 7.25** Shattering of water droplets of d = 1.0 mm for Ms = 1.58 in air at 1013 hPa, 288 K, at f = 150 Hz: **a** #83121602; **b** #83121504; **c** #83121405; **d** #83121503, single exposure; **e** #83121505; **f** #83121603; **g** #83121903, single exposure; **h** #83121509

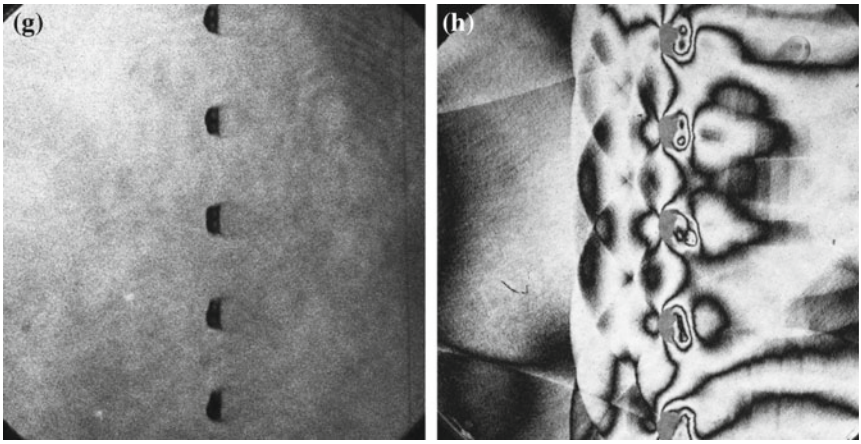


**Fig. 7.25** (continued)

As large diameter droplets can not be spherical, Hence, 4 mm diameter air containing droplets were produced by blowing water at slightly pressurized air from a co-axial nozzle and oscillating at frequency of 144 Hz (Yoshida and Takayama 1985). Figure 7.26 show sequential single exposure interferograms of 4 mm diameter air containing water droplets interacting with a shock wave of Ms = 1.68. The transmitted shock wave induced the boundary layer separation over the droplet surface. At the water droplet's rear side, a wake was formed and accelerated by a recirculation vortex. The shadow of such a disintegrating droplet reminded of the shape of a tadpole. The frontal side of the droplet was suppressed and gradually blown off toward downstream. It took about 1 ms for a droplet to be almost fragmented into mist. The particle velocity of the shock wave of Ms = 1.68 is about 310 m/s. The speed of mist particles ranges, presumably, 50–100 m/s.

In Fig. 7.27, the time variations of shattering droplets of different diameters d = 1.03 mm and 4.0 mm and shock wave of different Mach numbers for Ms = 1.3–1.5 are summarized (Wierzba and Takayama 1987). The ordinate denotes droplet diameter normalized by their initial diameters. The abscissa denotes dimension-less time $t^* = tu(\rho/\rho_l)^{1/2}/\mu$, where t, u, ρ, $\rho_l$, and μ are time, particle velocity, air density, liquid density, and viscosity, respectively. The circles are data collected by the present holographic interferometry. A solid line summarizes their distribution. A dotted line and a dot-and-point line summarize the previous data collected by means of conventional visualization. Upon impingement, droplets are bulged almost to maximal and then started contracting. The present holographic results suggest distinctly for shorter time than that offered in Reinecke and Waldmann (1975).

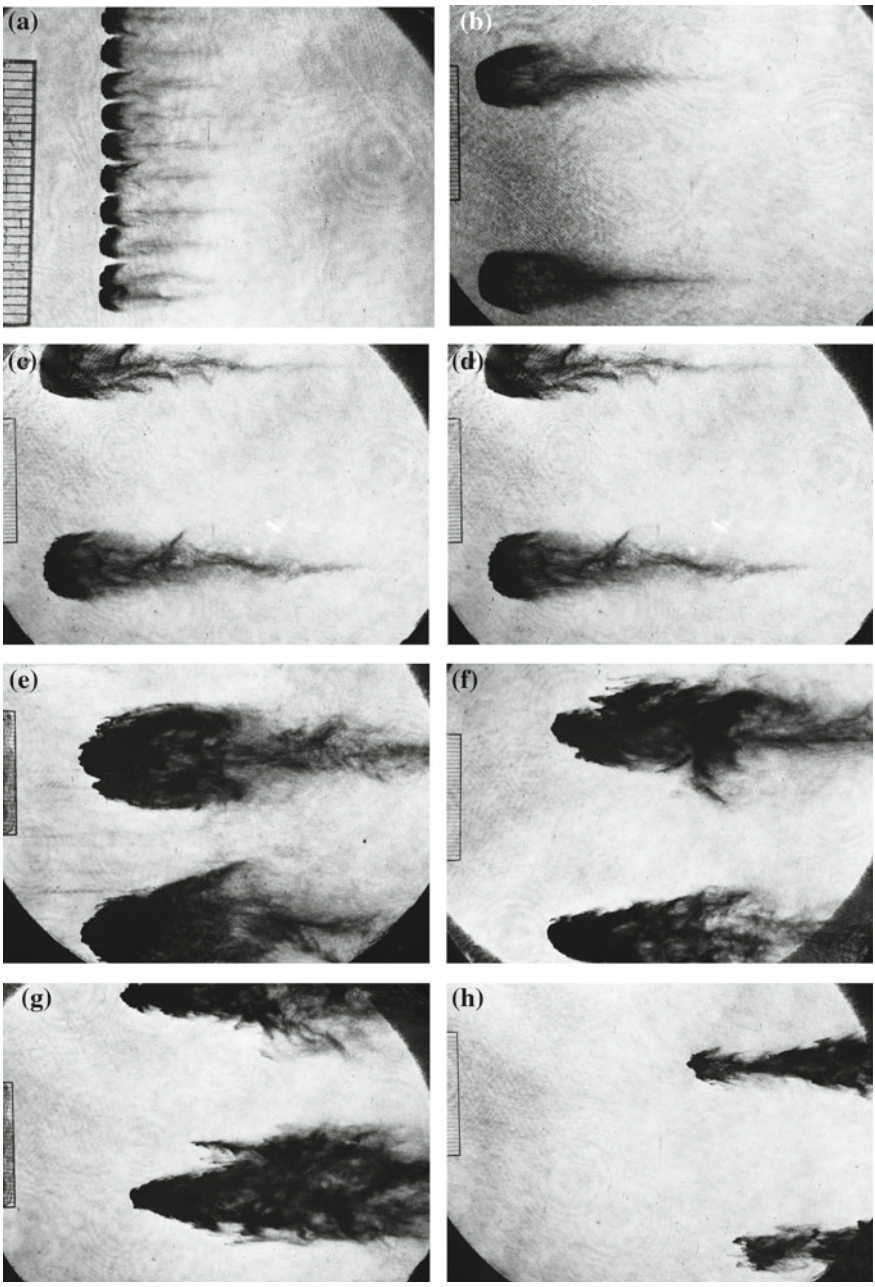


**Fig. 7.26** Shattering of water droplets of d = 4.0 mm for Ms = 1.68 in atmospheric air at 289.6 K, at f = 144 Hz, single exposure: **a** #86102809, 200 μs from trigger point, Ms = 1.680; **b** #86102511, 300 μs, Ms = 1.644; **c** #86102504, 400 μs, Ms = 1.660; **d** #86102503, 500 μs, Ms = 1.670; **e** #86102420, 600 μs, Ms = 1.656; **f** #86102507, 700 μs, Ms = 1.673; **g** #86102418, 800 μs, Ms = 1.671; **h** #86102505, 1150 μs, Ms = 1.644

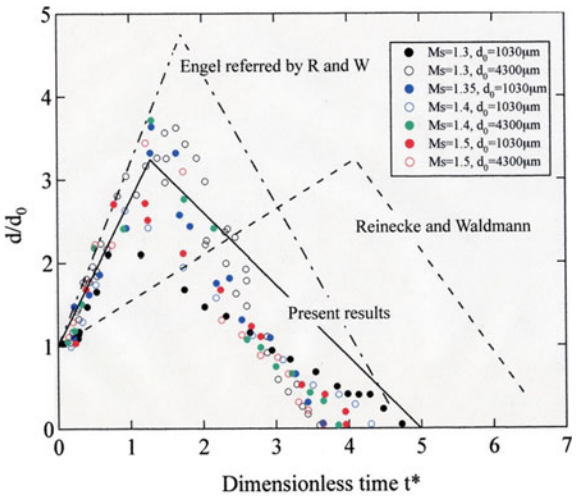


**Fig. 7.27** Time variations in of droplet's diameter, summary of experiments (Wierzba and Takayama 1987)

### *7.5.2 Shattering of Tandem and Triple Row Droplets*

Figure 7.28 show sequential visualization in the process of shattering 1.0 mm diameter water droplets, placed in 10 mm tandem position and dropped at 240 Hz frequency for Ms = 1.40 in atmospheric air. Figure 7.28b shows a double exposure interfrogram but all other photos are single exposure interferograms. Upon the shock wave loading, the droplets in the second row were exposed to the wake of droplets in the front row which have a lower relative speed. As seen in Fig. 7.28c–f, the droplets in the front row took over the droplets placed in the second row and eventually merged with each other as seen in Fig. 7.28e. Finally, the droplets in the first and second rows coalesced into a cloud as seen in Fig. 7.28f. In conventional shadow or schlieren photos, the shattering droplets appear as evenly illuminated grey expanding clouds, whereas in single exposure interferograms, the structures of shattering droplets are well resolved. The deviation of results shown in Fig. 7.26 was attributed to the inherited resolution of interferograms.

Figure 7.29 show shattering of 0.7 mm diameter ethyl alcohol droplets separated by 4 mm placed in triple rows and colliding with Ms = 1.25 shock wave in atmospheric air. Figure 7.29a, c are double exposure interferograms, in which blurred images are attributable to ethyl alcohol evaporation over the droplets. In Fig. 7.29e–g, three shattering droplets coalesced into one shattering droplet.

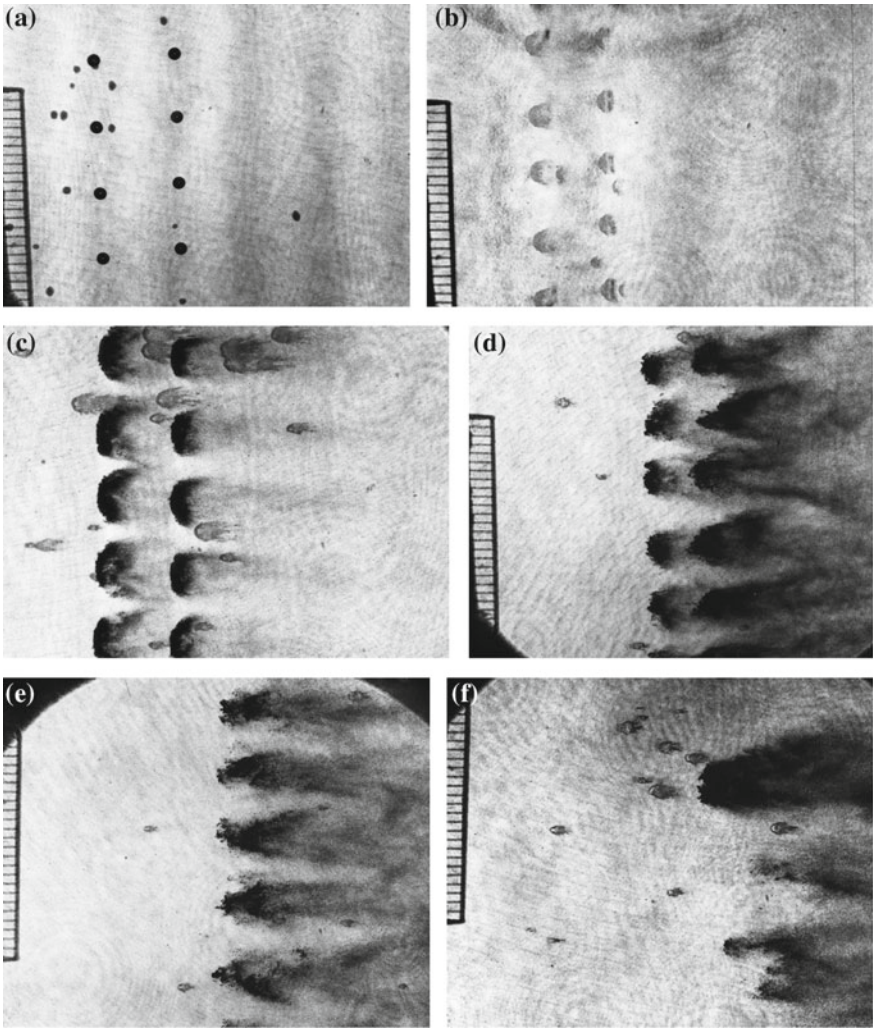


**Fig. 7.28** Shattering of 1.0 mm diameter tandem water droplets separated by 10 mm impinged by a Ms = 1.40 shock wave in atmospheric air, at 298.5 K at frequency 240 Hz, single exposure: **a** #87100201, no flow picture: **b** #87100206, 280 μs from trigger point, Ms = 1.389; **c** #87100202, 400 μs from trigger point, Ms = 1389; **d** #87100211, 600 μs, Ms = 1406; **e** #87100215, 700 μs, Ms = 1401; **f** #87100212, 0.8 ms, Ms = 1.400

## 7.6 Shock Wave Interaction with a Water Column

In earlier stage of the stripping type breakup, waves transmitted into liquid droplets and shock waves diffracting over the droplet surface promoted their deformations. In particular, the unsteady drag force promoted deformation and then accelerated

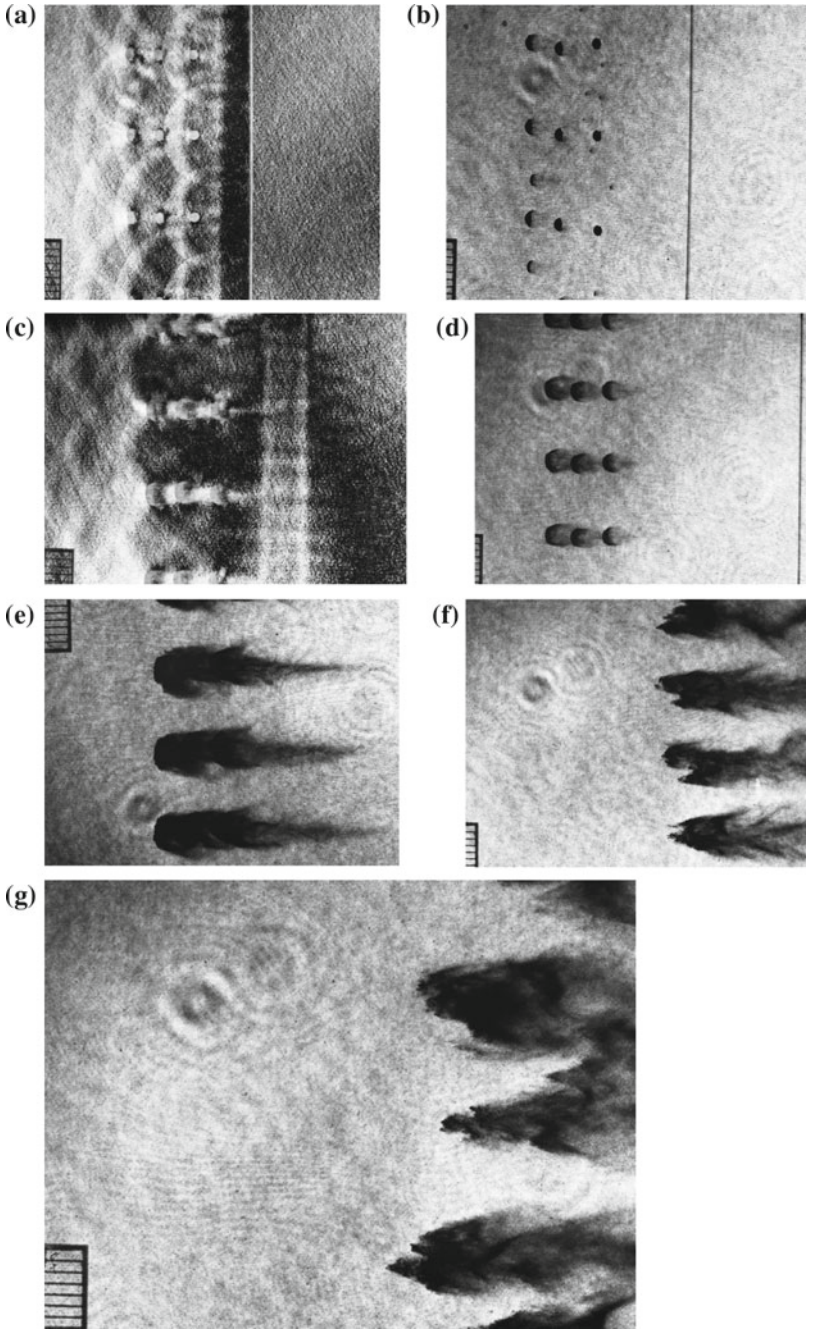
(a)
(b)
(c)
(d)
(e)
(f)
(g)

◂**Fig. 7.29** Shattering of 0.7 mm diameter triple row ethyl alcohol droplets separated by 4 mm for Ms = 1.250 in atmospheric air at 298.5 K. The droplets were dripped by three nozzles 4 mm interval at frequency 150 Hz: **a** #87040101, 250 μs from trigger point; **b** #87033116, 260 μs; **c** #87040102, 300 μs; **d** #87040103, 300 μs; **e** #87040104, 400 μs; **f** #87040113, 750 μs; **g** #87040108, 800 μs

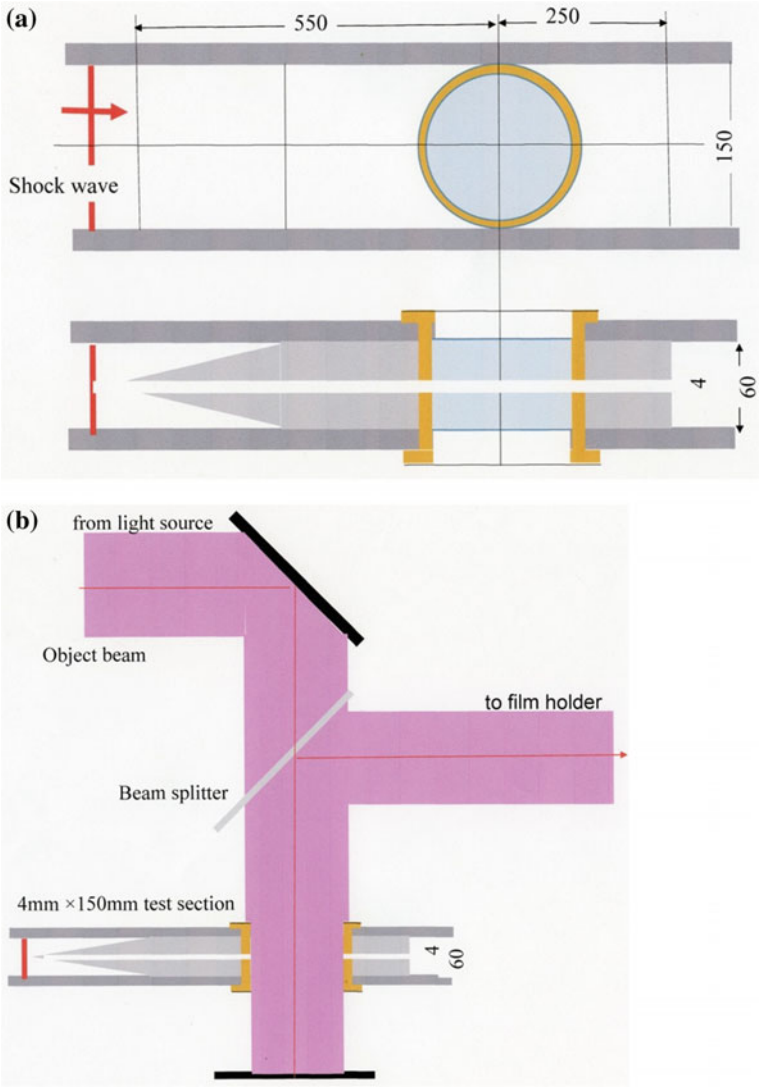


**Fig. 7.30** Water column experiment: **a** 4 mm × 150 mm test section; **b** optical arrangement (Yamada 1992; Shitamori 1990)

the droplet shattering. In a case of very small droplets and volatile liquids, evaporation would contribute significantly to the droplet fragmentation. Therefore, in order to understand the droplet deformation sequence, an analogue experiment was conducted. Figure 7.30a shows a 4 mm × 150 mm test section consisting of a cookie cutter and observation windows inserted in the 150 mm × 60 mm conventional shock tube; Hamamura (1995), Igra (2000).

Supplying water with a syringe needle at the center of the test section a water column having 4 mm in height and 6 mm in diameter was installed. Turning the test section sideway, the water column was visualized from its top. The shock wave hits the water column from its side.

Figure 7.30b shows the used optical arrangement. The observation windows were positioned horizontally. The collimated *OB* illuminated the test section vertically and reflected back from a plane mirror placed at the other side of the test section. It passed the test section again and reflected from a half mirror redirecting the *OB* toward the holographic film. With this optical arrangement, Fig. 6.30b formed the double path interferometry. The height of the tested water column was doubled, to 8 mm (Shitamori 1990).

Figure 7.31 show sequential observations of shock wave (Ms = 1.17), propagating in atmospheric air and interacting with a 6 mm diameter and 4 mm high water column. Figure 7.31a shows an early stage of interaction. In Fig. 7.31b–d, the shock wave was just propagating around the water column and reflected. With this arrangement, a fringe was observed inside the water column. In a single exposure interferogram, the boundary layer separation around the droplet's equator is observed; as seen in Fig. 7.31f, g. The observed separation zones remind observation of dust free regions seen in the Sect. 4.1.4 **Cylinder in dusty gas**. In double exposure intereferogram, the shadow of the initial water column and the motion of the shock wave in water are superimposed. Nevertheless, the reflection of the transmitted shock wave from the interface frontal surface of water/air bubble is visible in Fig. 7.31i.

Figure 7.32 show sequential single exposure interferograms of a water column interacting with a shock wave for Ms = 1.40 in atmospheric air.

Figure 7.33 summarized time variation during deformation of water column colliding with shock waves of Ms = 1.18–1.73 (Hamamura 1995). The ordinates in Fig. 7.33a denote time variations of the dimensionless longitudinal diameter, in Fig. 7.33b time variation of transversal diameter is shown, and in Fig. 7.33c, time variation of dimension-less mass, or in other words, the residual area of water column is presented. The abscissa is dimension-less time as defined in Fig. 7.27. In Fig. 7.33a the data points are plotted in a similar way as the solid line in Fig. 7.27. The longitudinal diameter increase with increasing time and reach its maximal value at $t^* \sim 25$. Thereafter it decreases monotonously and eventually vanishes at $t^* \sim 35$. The transversal diameter and the residual mass decrease monotonously and vanish at $t^* \sim 35$.

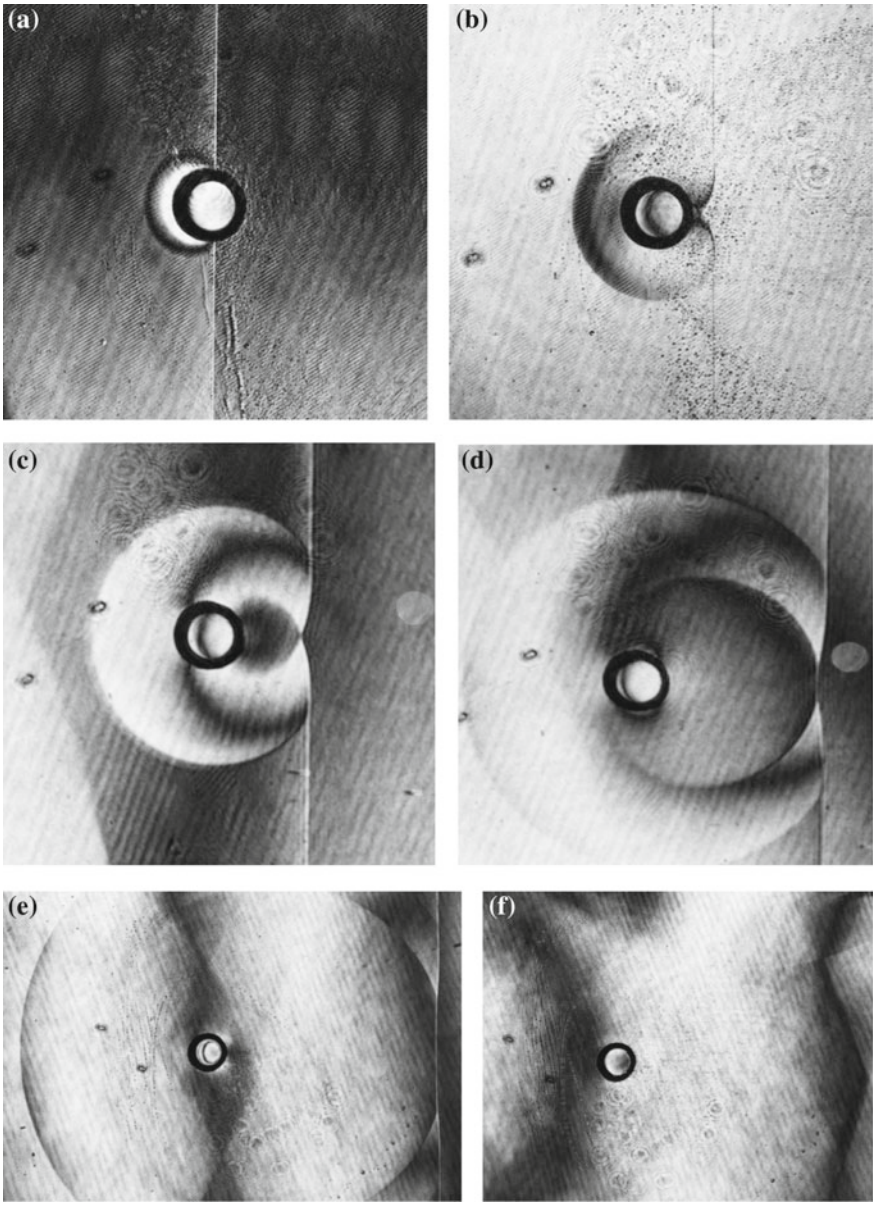


**Fig. 7.31** Evolution of 6 mm diameter water column exposed to a shock wave for Ms = 1.17 in atmospheric air at 296 K: **a** #89062807, 290 μs from trigger point, Ms = 1.170; **b** #89062807, 290 μs, Ms = 1.170; **c** #89062701, 315 μs, Ms = 1.173; **d** #89062703, 340 μs, Ms = 1.171; **e** #89062704, 390 μs, Ms = 1.17; **f** #89062705, 490 μs, Ms = 1.172; **g** #89062108, 590 μs, Ms = 1.169, single exposure; **h** #89062114, 630 μs, Ms = 1.169, single exposure; **i** #89062707, 690 μs, Ms = 1.169; **j** #89062708, 790 μs, Ms = 1.174; **k** 89062118, 790 μs, Ms = 1.169, single exposure; **l** #89062709, 890 μs, Ms = 1.172; **m** #89062120, 865 μs, Ms = 1.174, single exposure; **n** #89062801, 990 μs, Ms = 1.169; **o** #89062802, 990 μs, Ms = 1.173; **p** #89062124, 1040 μs, Ms = 1.171, single exposure; **q** #89062120, 865 μs, Ms = 1.174

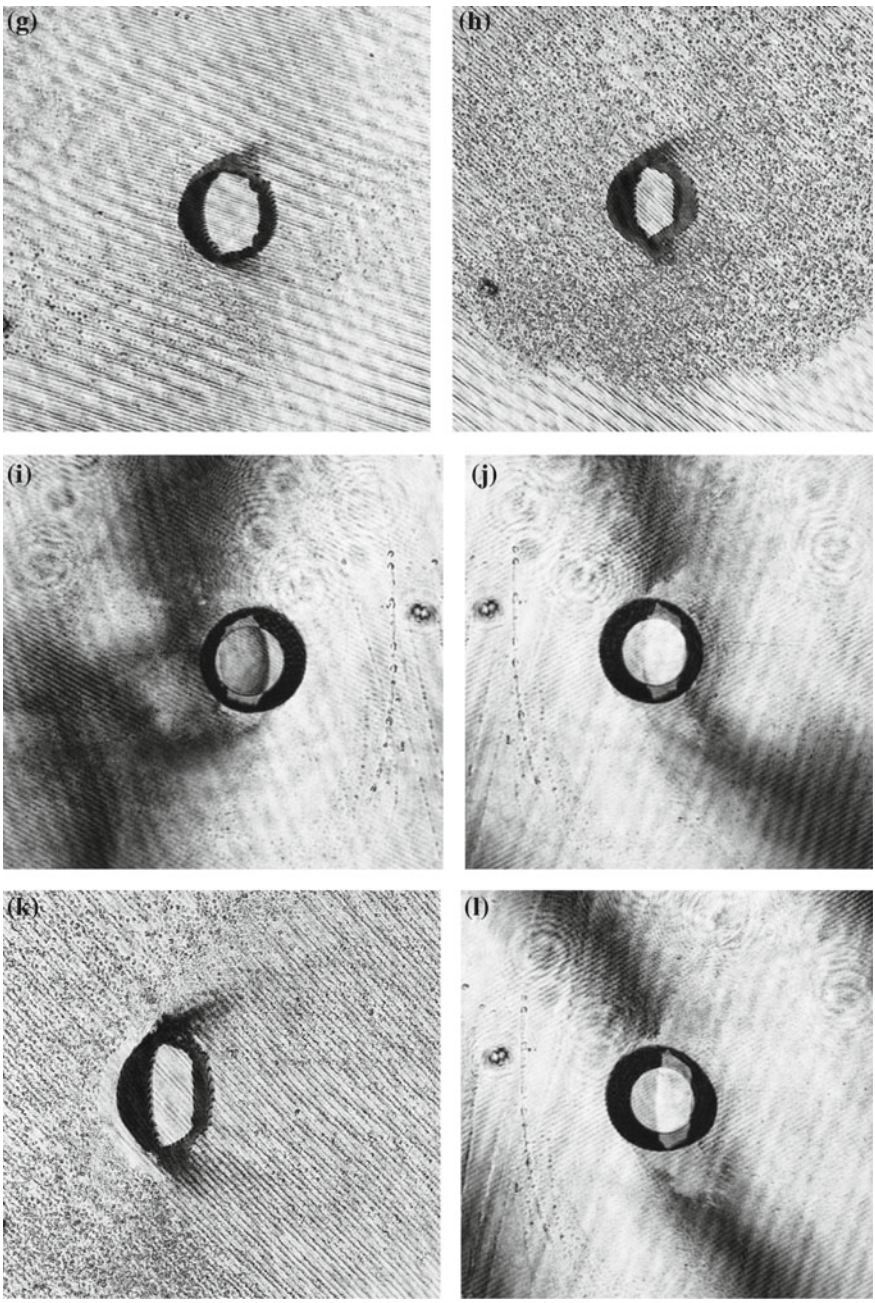


**Fig. 7.31** (continued)

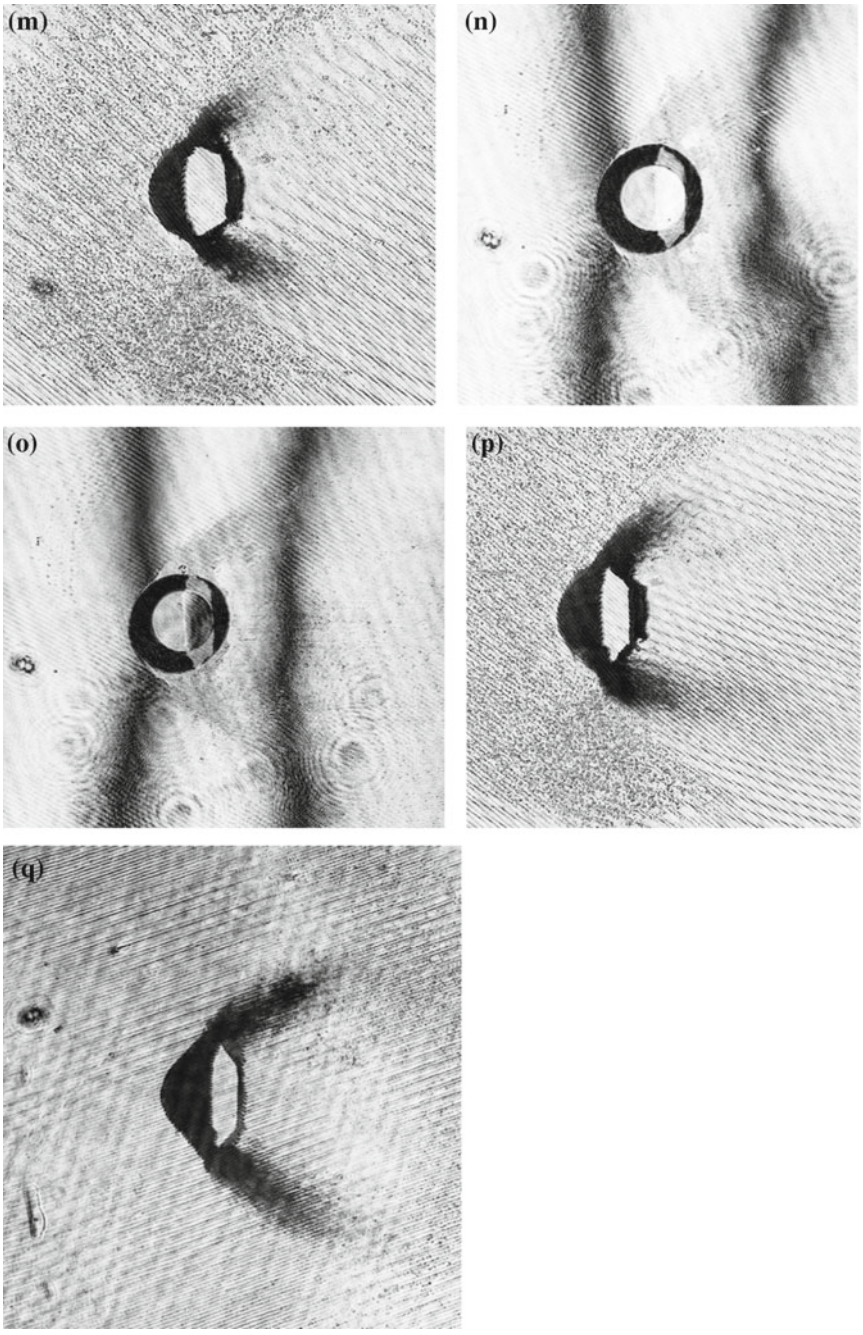


**Fig. 7.31** (continued)

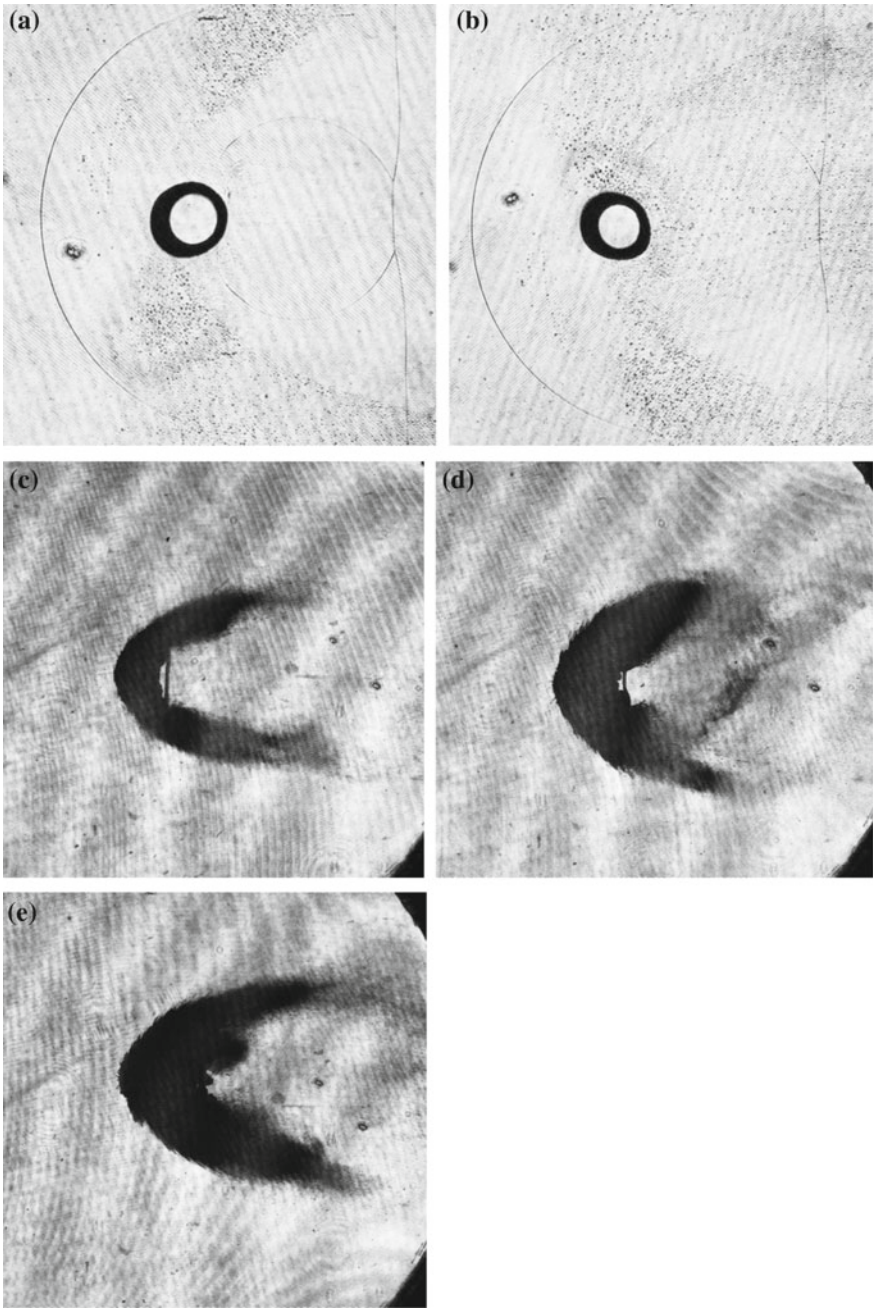


**Fig. 7.32** Single exposure interferograms of shock wave interaction with a 6 mm diameter water column for Ms = 1.4 in atmospheric air: **a** #89062814, 170 μs from trigger point, Ms = 1.457; **b** #89062812, 190 μs, Ms = 1.428; **c** #90071210, 780 μs, Ms = 1.440; **d** #90071206, 860 μs, Ms = 1.446; **e** #90071202, 920 μs, Ms = 1.420

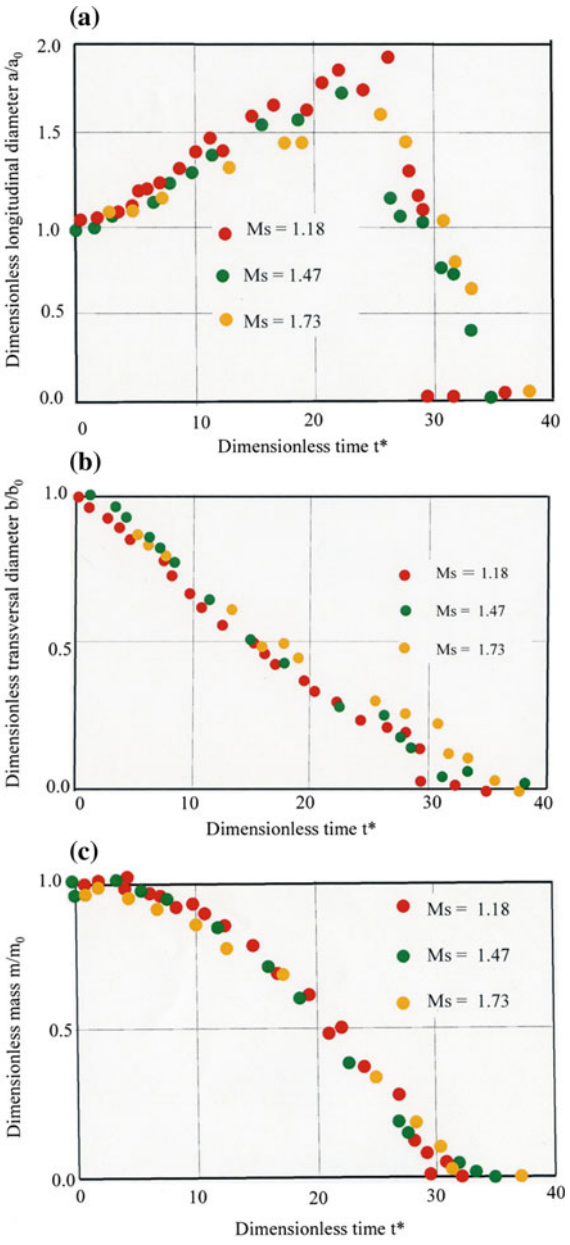


**Fig. 7.33** Time variation of water column deformation: **a** longitudinal residual diameter $a/a_0$; **b** transversal residual diameter $b/b_0$; **c** residual mass $m/m_0$ (Hamamura 1995)

### 7.6.1 Shock Wave Interaction with Tandem Water Columns

In order to simulate 1.0 mm diameter tandem water droplets separated by 10 mm as seen in Fig. 7.28, an analogue experiment was conducted by replacing the droplet with two water column. Figure 7.34a shows the arrangement and a so-called no flow picture. Two 6 mm diameter water columns were placed at 20 mm separation distance and shock wave of Ms = 1.45 will be loaded in atmospheric air. Figure 7.34b shows the earlier interaction. The first water column was deformed and shattered at first. Then the perturbed shock wave interacted with the second water so that the shock wave transferred the memory of the interaction with the first water column to the second water column and eventually the second water started to shatter. It was noticed that the fringes were visible inside the column. Probably the wave motion generated inside water columns might contribute to the boundary layer separation and hence to the early stage of their shattering. The air flew from left to right, at later time the drag force working on the first water column was larger than that on the second water column. Then in Fig. 7.28, with the elapsing time, two water droplets in tandem merged. However, the positions of the two water columns were fixed and could not move. The degree of shattering was distinctly different, which readily demonstrated the difference in the drag force as clearly see in Fig. 7.34i–l.

Figure 7.35 summarizes results of visualization presented in Fig. 7.34 for Ms = 1.45. The ordinate designates dimension-less residual mass and the abscissa designates dimension-less time t*. Red filled circles denote the second column, downstream column. Green filled circles denote the first column, upstream column. Orange color filled circles denote a single column exposed to shock wave of Ms = 1.45. The first column shatters very similarly to a single column. However, the second column collapses differently from the first column. This experiment was performed at the stand-off distance L = 20 mm. The stand-off distance would be a parameter which may control the shattering of the second water column. For very large L, the two water column would shatter independently. If the stand-off distance approaches the two water column may merge and collapse simultaneously.

**Fig. 7.34** Shattering of 6 mm diameter tandem water columns, L = 20 mm, Ms = 1.45 in ▶ atmospheric air at 300 K, single exposure: **a** #90071907, 150 μs from trigger point, Ms = 1.450, single exposure; **b** #90071907, 210 μs, Ms = 1.417; **c** #90071914, 240 μs, Ms = 1.450, single exposure; **d** #90072603, 270 μs, Ms = 1.443; **e** #90072604, 310 μs, Ms = 1.437; **f** #90072605, 380 μs, Ms = 1.447; **g** #90072310, 450 μs, Ms = 1.445, single exposure; **h** #90072314, 590 μs, Ms = 1.445, single exposure; **i** #90072316, 660 μs, Ms = 1.445, single exposure; **j** #90072402, 870 μs, Ms = 1.445, single exposure; **k** #90072410, 1120 μs, Ms = 1.442, single exposure; **l** #90072412, 1150 μs, Ms = 1.442, single exposure

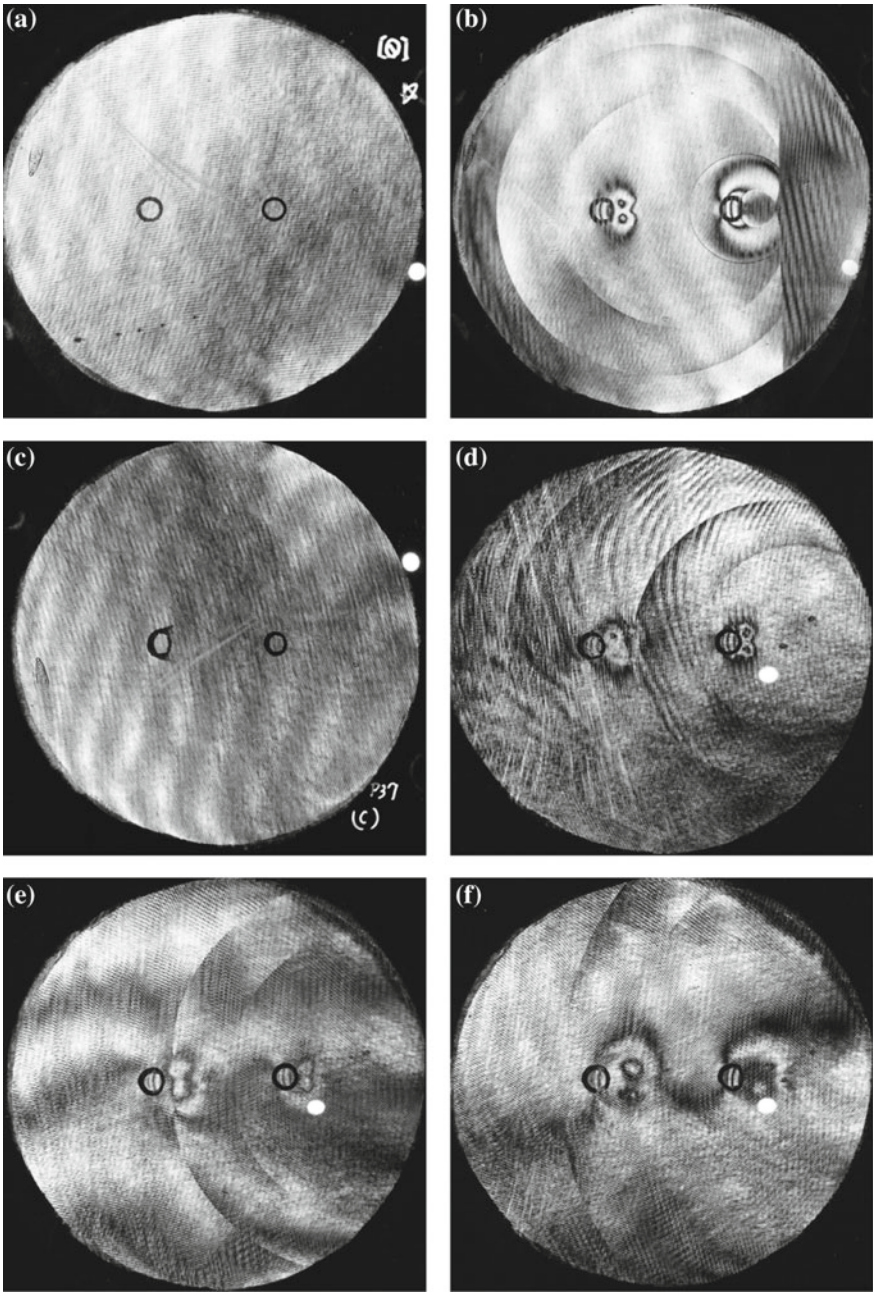
(a)
(b)
(c)
(d)
(e)
(f)

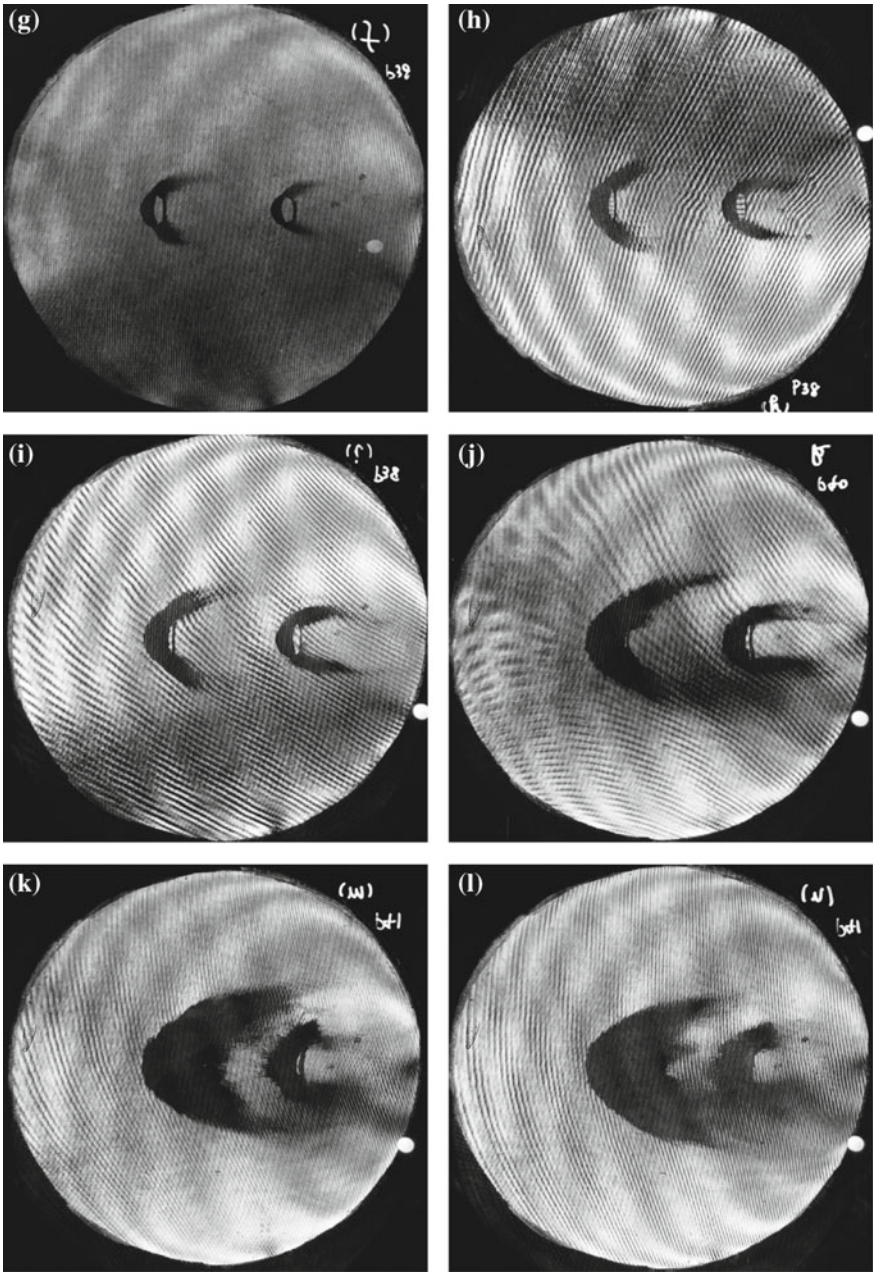


**Fig. 7.34** (continued)

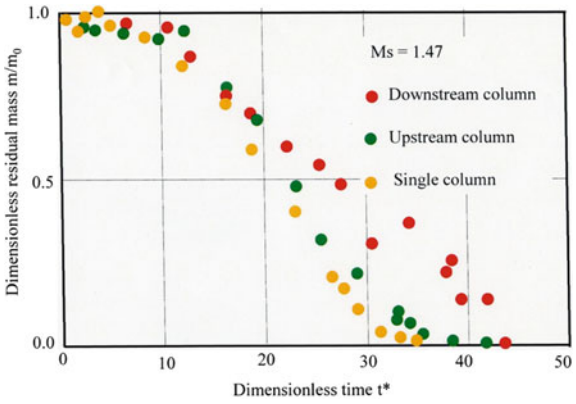


**Fig. 7.35** Time variation of residual mass $m/m_0$ of water columns in tandem (Hamamura 1995)

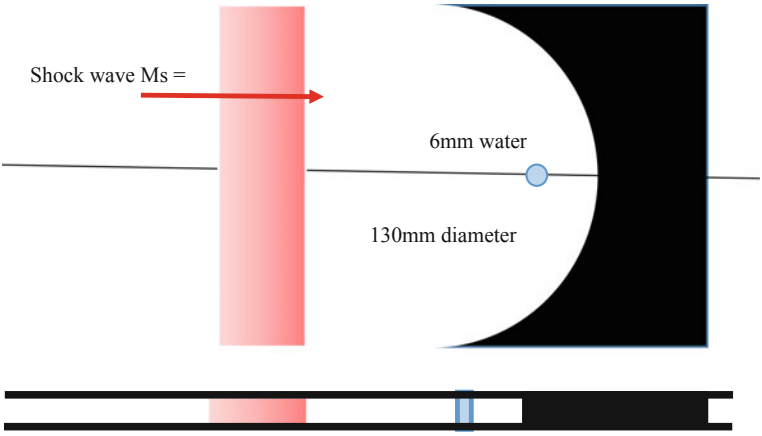


**Fig. 7.36** Shock wave focusing on a 6 mm diameter and 4 mm high water column (Hamamura 1995)

### *7.6.2 Interaction of Reflected Shock Wave with a Water Column Placed at Focal Point*

Figure 7.36 shows a 130 mm diameter and 4 mm wide circular reflector installed in a 60 mm × 150 mm conventional shock tube. This experiment is aimed at observation of the shattering of water column on which the shock wave of Ms = 1.45 is focused. The experimental condition is similar to the condition presented in Fig. 7.34.

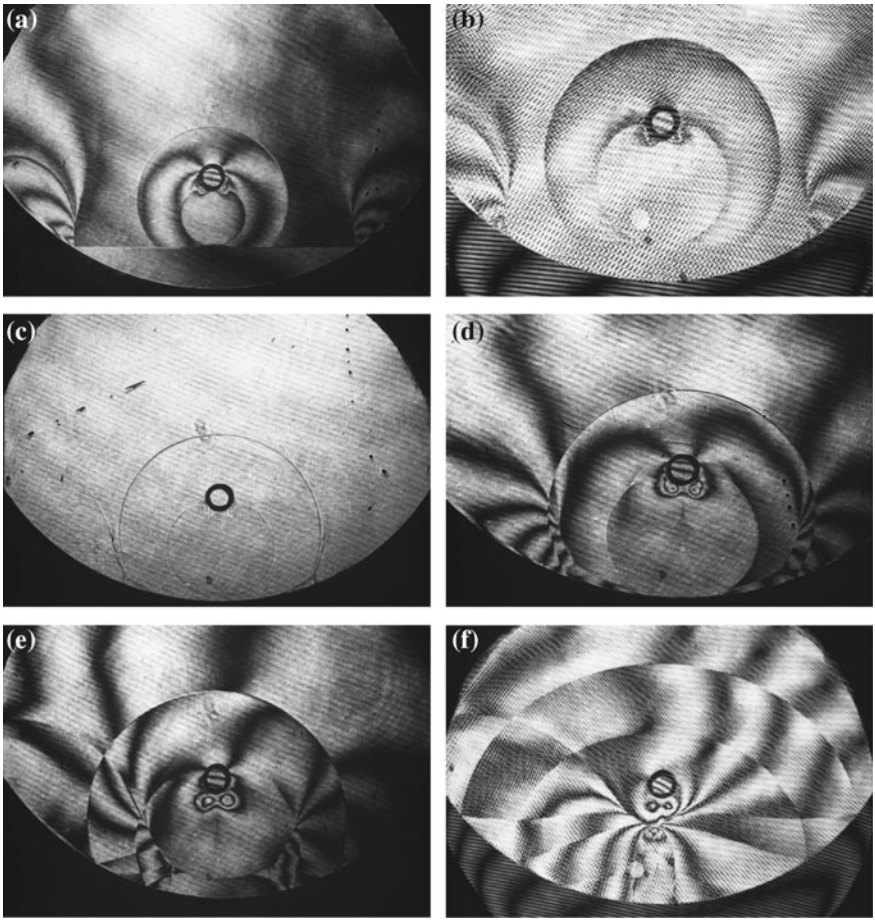


**Fig. 7.37** Disintegration of 4 mm high and 6 mm diameter water column exposed to shock wave focusing from a 130 mm diameter concave reflector for MS = 1.45 in air at 1013 hPa, 300 K: **a** #89101703, 160 μs from trigger point, Ms = 1.450; **b** #90070915, 200 μs from trigger point, Ms = 1.447; **c** #89102502, 200 μs Ms = 1.458, single exposure; **d** #89101704, 180 μs, Ms = 1.450; **e** #89101705, 200 μs, Ms = 1.450; **f** #90070914, 270 υs, Ms = 1.447; **g** #89102506, 280 μs, Ms = 1.458, single exposure; **h** #89102512, 420 μs, Ms = 1.458; **i** #89102516, 620 μs, Ms = 1.458, single exposure; **j** #89102518, 720 μs, Ms = 1.458, single exposure; **k** #90070919, 920 μs, Ms = 1.447, single exposure; **l** #90071810, 1720 μs, Ms = 1.438, single exposure (Hamamura 1995)

Figure 7.37 show sequential observations of deformation of the water column positioned at a focal point of a 130 mm diameter circular. At first, the incident shock wave interacted with the water column as seen in Fig. 7.36a, b, similarly to

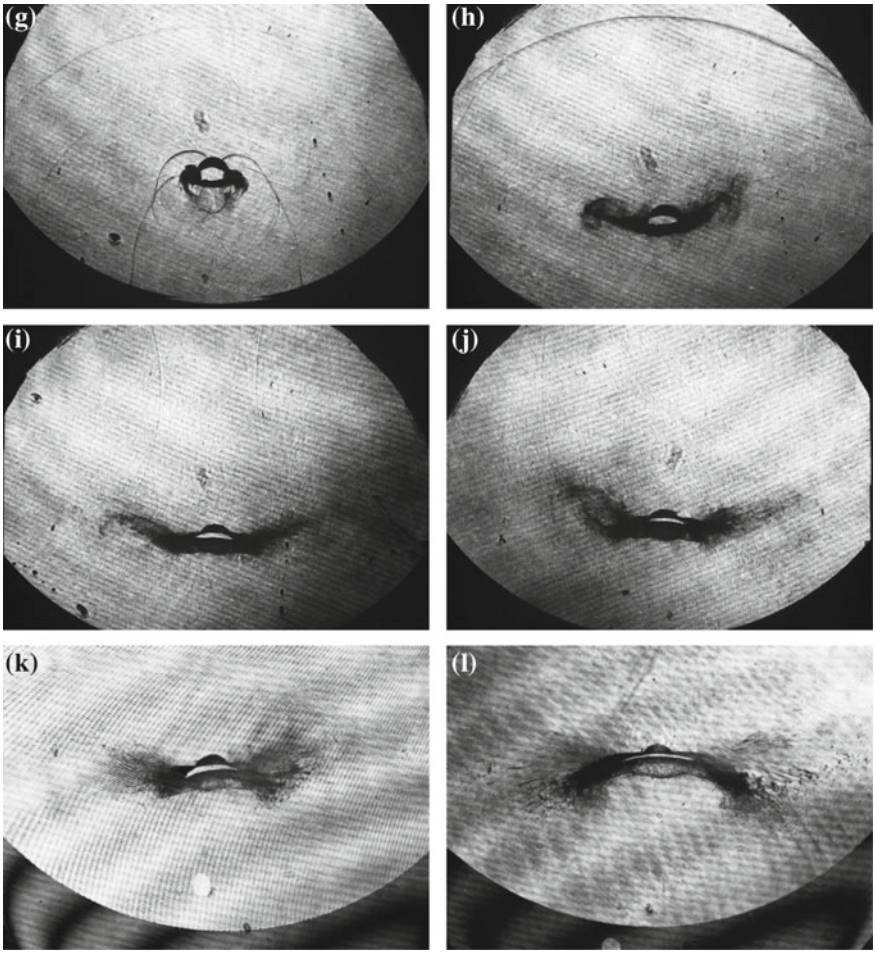


**Fig. 7.37** (continued)

the shock wave/solid cylinder interaction. Soon the waves converging towards the focus area and deform the column. The water column is exposed to high pressure at the focal region and then the column is deformed without casing any flow separation. The water column is squeezed from outside and deformed.

## References

Abd-el-Fattah, A. M., & Henderson, L. F. (1978). Shock wave at a fast-slow gas interface. *Journal of Fluid Mechanics, 86,* 15–32.

Gelfant, B. E., Silinikov, M. V., & Takayama, K. (2008). *Liquid droplet shattering*. Sanct Petersburg Technical University Press.

Hamamura, M. (1995). *Study of shock wave interaction with liquid column* (Master thesis). Graduate School of Engineering, Faculty of Engineering, Tohoku University.

Igra, D. (2000). *Experimental and numerical studies of shock wave interaction with gas-liquid interfaces* (Ph.D. thesis). Graduate School of Engineering, Faculty of Engineering, Tohoku University.

Matthujak, A. (2007). *Experimental Study of impact-generated high-speed liquid jets* (Ph.D. thesis). Graduate School of Engineering, Faculty of Engineering Tohoku University.

Nagoya, H. (1995). *Experimental study of Richtmyer-Meshkov instability* (Master thesis). Graduate School of Engineering, Faculty of Engineering, Tohoku University.

Pianthong, K. (2002). *Supersonic liquid diesel fuel jets generation, shock wave characteristics, auto-ignition feasibility* (Ph.D. thesis). School of Mechanical and Manufacturing Engineering, The University of New South Wales.

Reinecke, W. G., & Waldmann, G. D. (1975). *Shock layer shattering of cloud drops in reentry flight* (pp. 75–152). AIAA Paper.

Sachs, R. G. (1944). *The dependence of blast on ambient pressure and temperature*. BRL Report, No. 466.

Shi, H. H. (1995). *Study of hypersonic liquid jets* (Ph.D. thesis). Graduate School of Engineering, Faculty of Engineering, Tohoku University.

Shitamori, K. (1990). *Study of propagation and focusing of underwater shock focusing* (Master thesis). Graduate School of Tohoku University Faculty of Engineering, Tohoku University.

Tait, P. G. (1888). Report on physical properties of flesh and of sea water. Phys Chem Challenger Expedition, IV, 1–78.

Takayama, K., Onodera, O., & Esashi, H. (1982). Behavior of shock waves propagating along liquid surface. *Memoirs Institute High Speed Mechanics, Tohoku University, 419*, 61–78.

Yamada, K. (1992). *Study of shock wave interaction with gas bubbles in various liquids* (Doctoral Thesis). Graduate School of Tohoku University Faculty of Engineering, Tohoku University.

Yoshida, T., & Takayama, K. (1985). Interaction of liquid droplet and liquid bubbles with planar shock waves. In *International Symposium on Physical and Numerical Flow Visualization*, ASME.

Wierzba, A., & Takayama, K. (1987). Experimental investigation on liquid droplet breakup in a gas stream. *Report Institute of High Speed Mechanics, Tohoku University, 53*, 1–99.